INL/EXT-12-27568

# Long-Term Colloid Mobilization and Colloid-Facilitated Transport of Radionuclides in a Semi-Arid Vadose Zone

**Markus Flury**
**James B. Harsh**
**Fred Zhang**
**Glendon W. Gee**
**Earl D. Mattson**
**Peter C. Lichtner**

August 2012


The INL is a U.S. Department of Energy National Laboratory
operated by Battelle Energy Alliance

INL/EXT-12-27568

# Long-Term Colloid Mobilization and Colloid-Facilitated Transport of Radionuclides in a Semi-Arid Vadose Zone

Markus Flury[1]
James B. Harsh[1]
Fred Zhang[2]
Glendon W. Gee[2]
Earl D. Mattson
Peter C. Lichtner[3]

[1]Washington State University
[2]Pacific Northwest National Laboratory
[3]Los Alamos National Laboratory

August 2012

Idaho National Laboratory
Idaho Falls, Idaho 83415

http://www.inl.gov

Prepared for the
U.S. Department of Energy
Assistant Secretary for Environmental Management
Grant No. DE-FG02-08ER64660
Under DOE Idaho Operations Office
Contract DE-AC07-05ID14517

# FINAL REPORT
## U.S. Department of Energy

# LONG-TERM COLLOID MOBILIZATION AND COLLOID-FACILITATED TRANSPORT OF RADIONUCLIDES IN A SEMI-ARID VADOSE ZONE

**Principal Investigator:**

Markus Flury
Department of Crop and Soil Sciences
Washington State University

**Collaborators:**

James B. Harsh
Department of Crop and Soil Sciences
Washington State University

Fred Zhang
Pacific Northwest National Laboratory

Glendon W. Gee
Pacific Northwest National Laboratory

Earl D. Mattson
Geocentrifuge Laboratory
Idaho National Laboratory

Peter C. Lichtner
Geoanalysis—Earth and Environmental Sciences
Los Alamos National Laboratory

**Grant Number:**
DE-FG02-08ER64660

**Project Duration:**
September 1, 2008 to August 31, 2011
(no-cost extension until August 31, 2012)

# Contents

# 1 Executive Summary

The main purpose of this project was to improve the fundamental mechanistic understanding and quantification of long-term colloid mobilization and colloid-facilitated transport of radionuclides in the vadose zone, with special emphasis on the semi-arid Hanford site. While we focused some of the experiments on hydrogeological and geochemical conditions of the Hanford site, many of our results apply to colloid and colloid-facilitated transport in general. Specific objectives were (1) to determine the mechanisms of colloid mobilization and colloid-facilitated radionuclide transport in undisturbed Hanford sediments under unsaturated flow, (2) to quantify in situ colloid mobilization and colloid-facilitated radionuclide transport from Hanford sediments under field conditions, and (3) to develop a field-scale conceptual and numerical model for colloid mobilization and transport at the Hanford vadose zone, and use that model to predict long-term colloid and colloid- facilitated radionuclide transport.

To achieve these goals and objectives, we have used a combination of experimental, theoretical, and numerical methods at different spatial scales, ranging from microscopic investigations of single particle attachment and detachment to larger-scale field experiments using outdoor lysimeters at the Hanford site. Microscopic and single particle investigations provided fundamental insight into mechanisms of colloid interactions with the air-water interface. We could show that a moving air water interface (such as a moving water front during infiltration and drainage) is very effective in removing and mobilizing particles from a stationary surface. We further demonstrated that it is particularly the advancing air-water interface which is mainly responsible for colloid mobilization. Forces acting on the colloids calculated from theory corroborated our experimental results, and confirm that the detachment forces (surface tension forces) during the advancing air-water interface movement were

stronger than during the receding movement. Theory indicates that, for hydrophilic colloids, the advancing interface movement generally exerts a stronger detachment force than the receding, except when the hysteresis of the colloid-air-water contact angle is small.

We quantified the interaction forces (capillary forces) between colloids and the air-water interface by using force tensiometry. These measurements showed that capillary forces easily can exceed the attractive forces between colloids and the liquid-solid interface. Natural subsurface particles from the Hanford vadose zone where used for these measurements. Surface coatings and wetting conditions affect the magnitude of the capillary forces, but the most important parameter affecting the capillary force is the surface roughness and shape of the colloids. Irregularly-shaped particles with sharp edges showed the largest capillary forces, because the air-water interface gets pinned at edges. The implication of this phenomenon is that subsurface particles, which often contain edges and are irregularly shaped, are more readily mobilized than spherical model particles. This further emphasizes the important role of capillary forces in fate and transport of colloids in the vadose zone.

Field experiment using a vadose zone lysimeter facility at the Hanford site showed that surface-applied Eu colloids can be translocated rapidly under natural precipitation as well as artificial irrigation. Small amounts of applied colloids were translocated from the surface to a depth of two meters within two months and only 20 mm of cumulative infiltration. Large water infiltration events, mimicking snow melt, enhanced movement of Eu colloids. Nonetheless the majority of Eu colloids remained in the top 30 cm of the soil after 3.5 years of monitoring. These results suggest that colloid and radionuclide transport can occur in the near-surface vadose zone at Hanford under field conditions, but that the magnitude of the transport is less than what has been reported from laboratory studies.

Water flow rates in deep vadose zone sediments at Hanford vary from 0 to 100 mm/year.

We studied colloid mobilization from undisturbed sediment cores under a flow rate of 18 mm/year, a typical low flow rate at Hanford. Under this low flow rate, we observed continuous colloid mobilization from the sediments, although the total amounts of colloids mobilized are small, only 0.5% of available colloids were mobilized during 5 years of observations. These results demonstrate that colloidal particles are mobile even under the low recharge rates found in a semi-arid site like Hanford.

These results of our study are particularly relevant for colloid mobilization and transport related to three process in the vadose zone at Hanford: (1) water infiltration into sediments during rainfall or snowmelt events, (2) groundwater fluctuations as caused by river stage fluctuations, and (3) steady-state, low-flow recharge in deep vadose zone sediments. Transient water flow, like during infiltration or groundwater level fluctuations, are most conducive for colloid mobilization, but even during steady-state, low-flow recharge, colloids can be mobile, although to a much lesser extent. The results of this project have led to a comprehensive and fundamental understanding of colloid transport and mobilization under unsaturated flow conditions at the Hanford site.

## 2 Comparison of Actual Accomplishments with Goals and Objectives of the Project

*Objective 1: Determine the mechanisms of colloid mobilization and colloid-facilitated radionuclide transport in undisturbed Hanford sediments under unsaturated flow*

Mechanistic investigations of colloid mobilization and transport were conducted a different spatial scales, both experimentally as well as theoretically.

Systematic studies using confocal microscopy were conducted to determine how effective moving air-water interfaces are in mobilizing colloids from stationary surfaces. Investigations using a single cylindrical flow channel showed that the advancing air-water interface was significantly more effective in detaching colloids from the glass surface than the receding interface. Most of the colloids were detached during the first passage of the advancing air-water interface, while the subsequent interface passages did not remove significant amounts of colloids. Forces acting on the colloids calculated from theory corroborate our experimental results, and confirm that the detachment forces (surface tension forces) during the advancing air-water interface movement were stronger than during the receding movement. Theory indicates that, for hydrophilic colloids, the advancing interface movement generally exerts a stronger detachment force than the receding, except when the hysteresis of the colloid-air-water contact angle is small and that of the channel-air-water contact angle is large. The experiments and theoretical calculations also showed that there is a critical velocity of the air-water interface beyond which no colloids are removed anymore. This velocity is related to the expansion of the water film forming at the solid surface as water and air move through a capillary channel.

Colloids were modified to test the hypothesis that colloid shape has a dominant effect on colloid detachment. To make sure the differently shaped colloids had all the same surface properties, we modified spherical microspheres to form rods, barrels, ellipsoids, and disks. Barrels, which had an edge where the air-water interface was pinned, were removed the most by the moving air-water interface. The pinning of the air-water interface proved to be the most important factor leading to increased colloid removal and mobilization.

Force tensiometry was used to quantify capillary forces as a function of position of the air-water interface on model and natural particles. We have shown that capillary forces exerted at the air-water interface can exceed DLVO and gravity forces, and that moving air-water interfaces during infiltration can mobilize, i.e., detach, soil particles from stationary surfaces. In porous media, while under dry conditions, the capillary force is a strong attachment force of particles to stationary surfaces, under wet conditions, the capillary force becomes a mechanism of detachment of particles from stationary surfaces. Such wet conditions occur during infiltration or drainage. We quantified such detaching capillary forces for differently shaped particles and found that measured capillary forces on natural particles can be approximated by a volume-equivalent ellipsoid. Thus, assuming

an ellipsoidal shape allows us to better predict capillary forces experienced by natural particles in porous media. Capillary forces become more important the smaller the particles are, because the gravity force decreases faster with particle size than the capillary force, and the capillary pressure scales inversely with the particle radius. Thus, particularly for particles in the colloidal size range, the capillary forces will play a dominant role.

Theory was developed to calculate the capillary forces based on particle shape. For non-symmetrical particles, the calculation of the capillary force requires consideration of undulating interface lines, making the the theory complex and involved. The theory allows to approximate natural subsurface particles as volume-equivalent ellipsoids.

*Objective 2: Quantify in situ colloid mobilization and colloid-facilitated radionuclide transport from Hanford sediments under field conditions*

A field experiment was conducted to quantify transport of an intrinsic radionuclide colloid at the Hanford site. As a surrogate for intrinsic Am and Eu colloids, we used non-radioactive Eu-hydroxy-carbonate colloids, $Eu(OH)(CO_3)$. The colloids were applied to the surface of field lysimeters and migration of the colloids through the sediments was monitored using wick samplers. The lysimeters were exposed to natural precipitation or artificial irrigation. Wick outflow was analyzed for Eu concentrations and particle counts, supplemented by electron microscopy and energy-dispersive x-ray analysis on selected samples. Small amounts of Eu colloids were detected in the deepest wick sampler (2.14 m depth) 2.5 months after application and cumulative precipitation of only 20 mm. We observed rapid transport of Eu colloids under both natural precipitation and artificial irrigation, i.e., the leading edge of the Eu colloids moved at a velocity of 3 cm/day within the first two months after application. Large water infiltration, mimicking Chinook snowmelt events in late winter/early spring, caused peaks of Eu in the wick outflow. Elevated Eu concentrations were detected in 1.22 and 2.14 m depth 2.5 years after application, which is consistent with long-term recharge estimates at the site. However the main mass of Eu remained in the top 30 cm of the soil. The observed rapid movement of Eu in the homogeneous Hanford Lysimeters was caused by transient water flow near the soil surface. Based on mechanistic laboratory studies, it is likely that the Eu colloids were mobilized and translocated by moving air-water interfaces. The main peak of Eu, however, moved at slower rate, consistent with long-term recharge.

To investigate whether the in situ natural colloids can be mobilized and transported in undisturbed, deep vadose zone sediments at the Hanford site under typical, semi-arid recharge rates, we used an undisturbed sediment core. We sampled an undisturbed sediment core (50 cm i.d., 59.5 cm height) from a depth of 17 m at the Hanford 200 Area. The core was setup as a laboratory lysimeter and exposed to a low infiltration rate of 18 mm/year by by applying simulated pore water onto the surface. Particle concentrations were quantified in the column outflow, and selected samples were examined microscopically and for elemental composition (TEM and EDX). Measured water contents and potentials

were used to calibrate a numerical model (Hydrus-1D), which was then applied to simulate colloid mobilization form the sediment core. The results showed that during 5.3 years of monitoring, natural colloids like silicates, aluminosilicates, and Fe-oxides were observed in the core outflows indicating the continuous mobilization of in situ colloids. The total amount of particles mobilized within 5.3 years corresponded to 0.5% of the total dispersible colloids inside the core. The fitted release rate coefficient was six to seven orders of magnitude smaller than coefficients reported from previous studies, where disturbed Hanford sediments and higher flow rates were used. Our findings demonstrate that even under low recharge rates and water contents typical for semi-arid, deep vadose zone sediments, particles can continuously be mobilized, although the total mass of particles is low.

*Objective 3: Develop a field-scale conceptual and numerical model for colloid mobilization and transport at the Hanford vadose zone, and use that model to predict long-term colloid and colloid-facilitated radionuclide transport*

Colloid and colloid-facilitated contaminant transport mechanisms have been incorporated into the multiphase flow and transport model PFLOTRAN. Our results demonstrate that under field conditions with transient flow, colloid mobilization and transport occurs in Hanford sediments. Small amounts of Eu colloids could be translocated by natural precipitation or irrigation to a depth of 2.14 m within 2.5 months, corresponding to an overall colloid transport velocity of 3 cm/d. Estimates of recharge at the Hanford site range from 1 to 100 mm/year. Considering a volumetric water content of 0.1 $m^3/m^3$, the recharge estimates translate to a pore water velocity of 1 to 100 cm/year (equal to 0.003 to 0.3 cm/d), which is considerably slower than what we observed based on the fast Eu transport. This indicates that the near surface transport of a portion of Eu can be rapid, exceeding recharged-based velocity estimates by more than a factor of ten. While a small portion of Eu colloids moved rapidly by preferential flow, the main peak of Eu, however, moved at slower rate, consistent with long-term recharge.

While semi-arid conditions in general are not conducive for colloid transport, the dry summer and wet winter climate at the Hanford site leads to infiltration fronts that penetrate the soil to several meters. These infiltration fronts with their associated moving air-water interfaces provide a means for mobilization and transport of colloids in the near-surface vadose zone.

In the deep vadose zone, we had the premise that particle mobilization is hindered under the low water contents and low steady-state flow rates. However, we did observe continuous particle release. Our study showed that in situ colloid mobilization occurred at a steady-state flow rate of 0.05 mm/d (= 18 mm/y) in an undisturbed sediment core. Although release rate and mass recovery of particles were much lower than reported from previous studies where colloid mobilization from disturbed, sediment columns was reported, we did observe a continuous flux of particles leaving the sediment core.

Our results show that in semi-arid regions, the thick vadose zone with its low water content and flow rates does not necessarily constitute a perfect filter for particle transport. Even under low, steady-state flow rates, particles were mobilized. The continuous particle mobilization observed here may be a possible pathway for colloid-facilitated contaminant transport at the US DOE Hanford site.

# 3 Summary of Project Activities

This section provides a summary of the experimental methods and results of the project. A detailed account of these activities is given in the attached technical manuscripts in the Appendix.

## 3.1 Motivation

Radioactive wastes stores at Hanford and other nuclear facilities pose a threat to the environment when waste are accidentally released. Knowledge of fate and transport of waste constituents is a requirement for effective clean-up and long-term management of contaminated sites. While some contaminants, like Cs, Am, Pu, sorb strongly to soil and sediment surfaces and are therefore expected to be retained near the location of their release, it has been shown that colloidal particles can facilitate the movement of these contaminants if the contaminants either associate with the colloids or form colloids themselves. Research from laboratory experiments has shown that colloids can be mobilized from soils and sediments under unsaturated and transient flow. How far-reaching and effective this process is for radionuclide migration in the *vadose zone* at Hanford, however, is not known. In this project we addressed the following major question: How effective are colloids in enhancing the mobility of radionuclides in the Hanford vadose zone, and what is the *long-term* magnitude of this transport process?

## 3.2 Research Objectives

The general goal of this project was to improve the fundamental mechanistic understanding and quantification of long-term colloid mobilization and colloid-facilitated transport of radionuclides in the vadose zone, with special emphasis on the semi-arid Hanford site. The specific objectives were to:

1. Determine the **mechanisms** of colloid mobilization and colloid-facilitated radionuclide transport in undisturbed Hanford sediments under unsaturated flow.

2. Quantify *in situ* colloid mobilization and colloid-facilitated radionuclide transport from Hanford sediments under **field conditions**.

3. Develop a field-scale conceptual and numerical model for colloid mobilization and transport at the Hanford vadose zone, and use that model to predict **long-term** colloid and colloid-facilitated radionuclide transport.

## 3.3 Overall Research Design

The objectives of this study were accomplished through a combination of experimental, theoretical, and numerical investigations at different spatial and temporal scales. Spatial scales ranged from microscopic scale, single particle scale, column scale, to the field scale. At the microscale and single particle scale, we used microscopic and tensiometric techniques to elucidate fundamental mechanistic interactions of colloids with the air-water interface. At the column scale, we used (1) a geocentrifuge to separate effects of flow rates and water contents on colloid mobilization, and (2) an undisturbed sediment core to quantify long-term colloid mobilization under flow rates typical for the low recharge in the deep Hanford vadose zone. At the field scale, we studied Eu-colloid transport in several lysimeters located at the Hanford site under natural and artificial precipitation. Theoretical and numerical models were used to analyze and generalize the experimental data.

## 3.4 Mechanistic Investigations on Colloid Transport in Unsaturated Porous Media

### *3.4.1 Colloid Interactions with Air-Water Interface*

(*References:* Aramrak et al., 2011; Aramrak et al., 2012)

**3.4.1.1 Motivation** Previous experiments have shown that when water infiltrates or drains from soil or sediment, colloidal particles tend to be mobilized and leached as the infiltration or drainage fronts moves through the medium. We hypothesized that it is the interaction of the colloids with the moving air-water interface that is responsible for the colloid mobilization.

**3.4.1.2 Materials and Methods** To determine how effective moving air-water interfaces are in detaching colloids from surfaces, we deposited fluorescent, negatively-charged, carboxylate-modified polystyrene colloids (diameter of 1 $\mu$m) into a cylindrical glass channel. Hydrophilic carboxylate-modified microspheres (FluoSpheres, Lot Number 28120W, Molecular Probes Inc., Eugene, OR) were selected as the colloid models. The microspheres had a specific density of 1.055 g/cm$^3$ and surface charge of 0.0175 mol$_c$/g (Molecular Probes Inc., Eugene, OR). The colloids were hydrophilic with an advancing air-water contact angle of 60 degrees and a receding contact angle of 40 degrees. After colloid deposition, two air bubbles were sequentially introduced into the glass channel and passed through the channel at different velocities (0.5, 7.7, 72, 982, and 10,800 cm/h). The passage of the bubbles represented a sequence of receding and advancing air-water interfaces (Figure 1). Colloids remaining in the glass channel after each interface passage were visualized with confocal microscopy and quantified by image analysis (Figure 2). To check whether the colloids removed by the moving air-water interfaces were initially deposited in the secondary

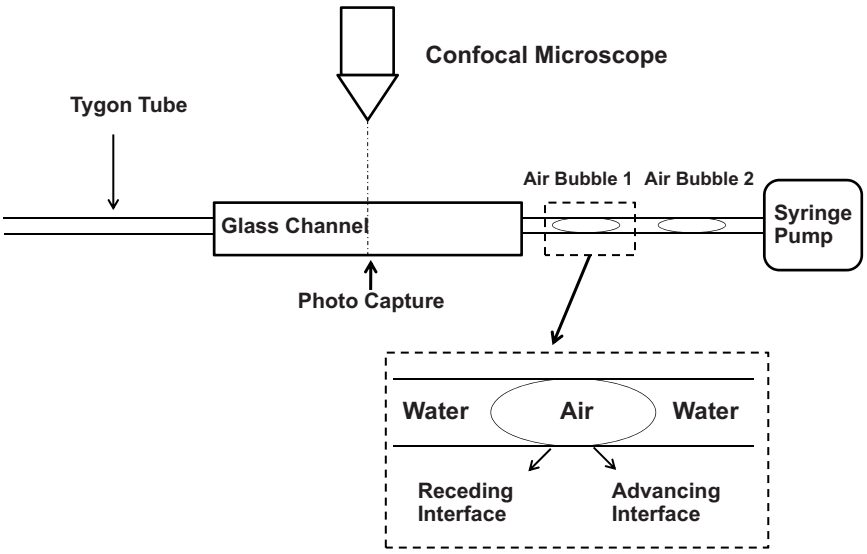


Figure 1. Schematic of experimental setup for air-water interface displacement.

energy minimum (i.e., unfavorable condition) or primary energy minimum, we conducted another set of experiments by changing the solution chemistry. We calculated an appropriate solution chemistry using DLVO theory to determine a solution that will cause the secondary minimum to disappear. We calculated an appropriate solution chemistry using DLVO theory to determine a solution that will cause the secondary minimum to disappear. We deposited the colloids into the channel as described above and then changed the solution chemistry to 0.1 mM $CaCl_2$ and pH 4.7. Visualization and quantification of colloids deposited on the glass channel was done before and after changing the solution chemistry at all the specific velocities indicated above.

To determine the effect of particle shape on colloid removal, we modified polystyrene colloids to form rods, elliptical disks, and barrels, plate-like, and edge-shaped natural particles. The different shapes were made by encasing microspheres into a film of polyvinyl alcohol (PVA), liquifying the microspheres with either hot oil or toluene, and stretching this film to different aspect ratios using a material tension tester.

Theoretical calculations were performed to determine the expected detachment forces a well as the thickness of the water film as a function of flow velocity. Calculations showed a strong dependence of the detachment forces as a function of contact angle. Calculated shear forces were found to be insignificant compared to detachment forces. We also calculated

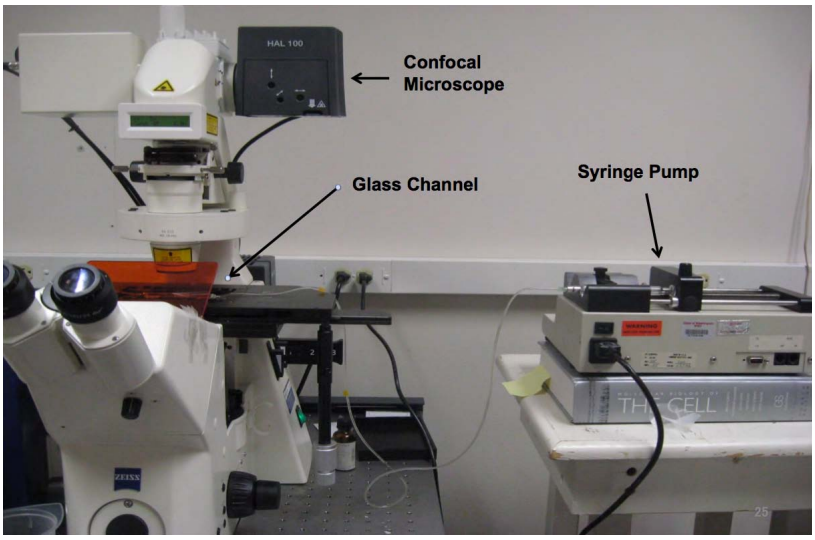


Figure 2. Experimental setup to quantify colloid detachment by moving-air-water interfaces.

contact and induction times during colloid and air-water-interface interactions, i.e., the time it takes for the air-water interface to form a colloid-water-air interface line with a colloid when the air-water interfaces approaches the colloid.

**3.4.1.3 Principal Results** A typical sequence of confocal images showing colloid deposition and detachment after receding and advancing air-water interface movements is shown in Figure 3. The initial spatial distribution of the colloids on the glass surface represents our reference from which we calculated colloid detachment. After passage of the receding air-water interface, more colloids are visible upstream of the interface, and we consider these colloids being attached the thinning air-water interface trailing the interface front. We could identify the interface location optically because the colloids viewed through water and air phases had different brightness in the confocal microscope. After passage of the advancing air-water interface, only a small fraction of colloids were removed. The following advancing air-water interface showed a pronounced accumulation of colloids at the interface, and after passage of the interface, a large fraction of colloids were removed from the glass surface.

Table 1 shows the quantitative amounts of colloids detached after passage of the air-water interfaces as a function of interface velocity. The hydrodynamic force caused by the flow itself was not able to remove colloids from the glass surface at any velocity, as no colloids were removed during flow in absence of an air bubble, and the surface tension force indeed was the dominant force causing colloid detachment. Colloid detachment was most pronounced at low flow velocities (1, 10, and 100 cm/h). The majority of the colloids

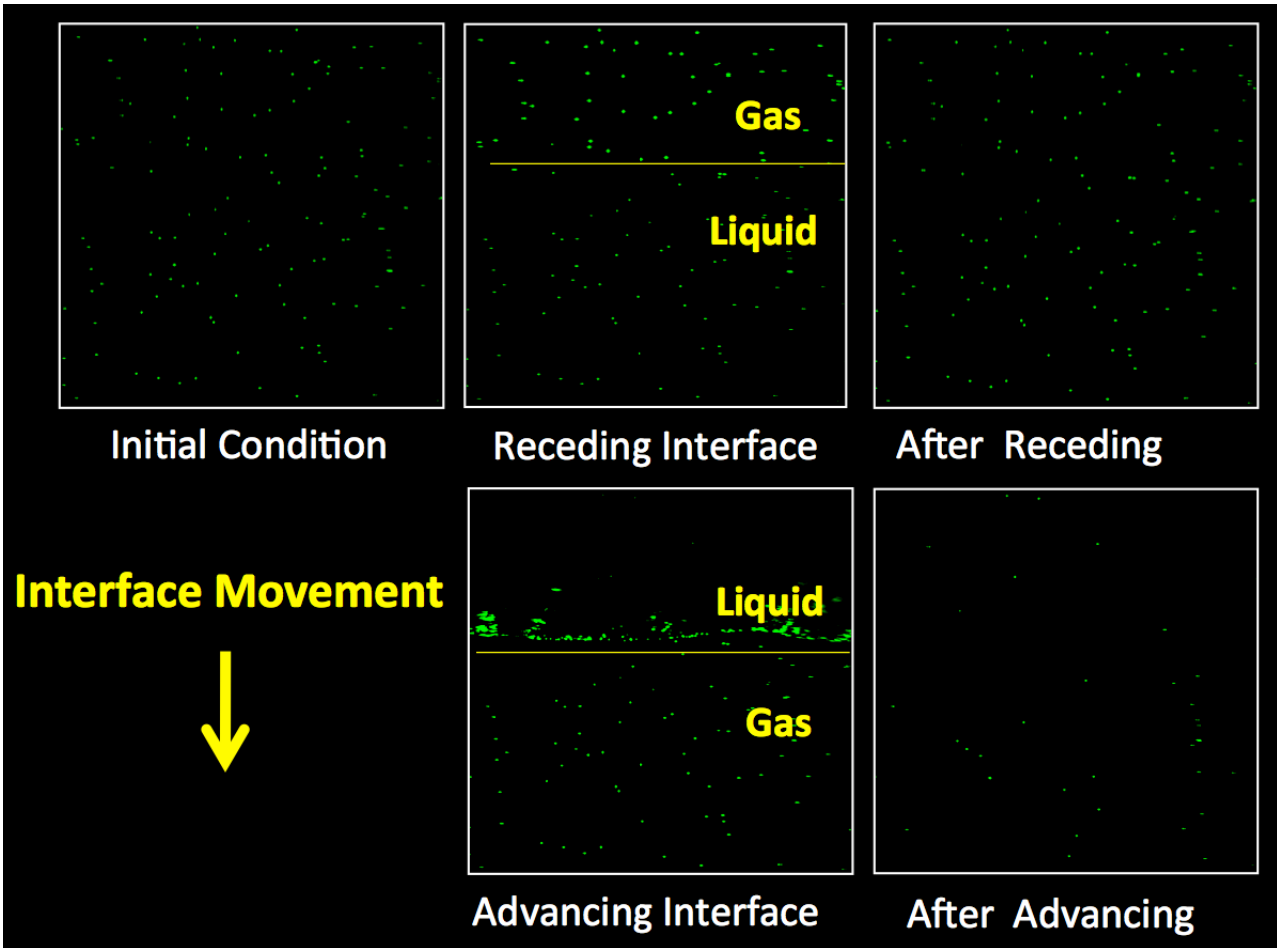


Figure 3. Sequence of confocal images showing colloids deposited on a glass channel before, during, and after air-water interface movements.

Table 1. Colloid detachment (%) from a glass surface after the passages of air-water interfaces.

| | Colloid detachment (%) at different velocities | | | | |
|---|---|---|---|---|---|
| | 1 (0.5)* | 10 (7.7) | 100 (72) | 1000 (982) | 10000 (10,800) |
| | (cm/h) | | | | |
| Initial state | 0 Aa | 0 Aa | 0 Aa | 0 Aa | 0 Ab |
| Flow (no bubble) | 0Aa | $0.01 \pm 0.01$ Aa | $0.01 \pm 0.01$ Aa | $0.02 \pm 0.02$ Aa | $0.02 \pm 0.03$ Ab |
| After receding-1 | $5 \pm 6$ Aa | $5 \pm 5$ Aa | $9 \pm 6$ Aa | $2 \pm 4$ Aa | $0.4 \pm 0.7$ Ab |
| After advancing-1 | $88 \pm 10$ Ba | $85 \pm 10$ Ba | $80 \pm 6$ Ba | $72 \pm 28$ Ba | $1 \pm 2$ Bb |
| After receding-2 | 0 Aa | 0 Aa | $0.2 \pm 0.5$ Aa | $1 \pm 2$ Aa | $0.1 \pm 0.3$ Ab |
| After advancing-2 | $3 \pm 5$ Aa | $2 \pm 4$ Aa | $2 \pm 2$ Aa | $12 \pm 21$ Aa | $0.1 \pm 0.3$ Ab |

* Numbers in parentheses are measured velocities. Data represent means and standard deviations measured from 12 replications. Different capital letters (A, B, and C) indicate statistical differences column-wise; and different lower cases (a, b, and c) indicate statistical differences row-wise; both at $\alpha = 0.01$.

were removed by the first advancing interface (advancing-1), and no significant difference in colloid detachment was observed among the three lowest velocities of 1, 10, and 100 cm/h. Indeed for all interface passages, the amounts of colloids detached were not a function of interface velocities in the range of 1 to 100 cm/h; however, for faster velocities (1,000 and 10,000 cm/h), colloid detachment drastically decreased.

Shape-modified colloids showed a preference for removal of colloids with edges (barrels and disks) (Figure 4). The advancing air-water interface was much more effective in removing colloids than the receding interface. Interestingly, even the receding interface could not remove colloids, no matter what shape the colloids had.

### *3.4.2 Capillary Forces between Particles and the Air-Water Interface*

(*References:* Chatterjee et al., 2012)

**3.4.2.1 Motivation** In these experiments, we quantified the capillary forces (surface tension forces) acting on natural subsurface particles. No experimental and theoretical quantification of the capillary forces for natural particles have been reported to date, and our data show that the capillary force is a dominant force. We generalize the results by also using a series of standard shaped model particles.

**3.4.2.2 Materials and Methods** The particles were collected from 20 m depth from a trench face at the Hanford Environmental Restoration Disposal Facility, located 13 km

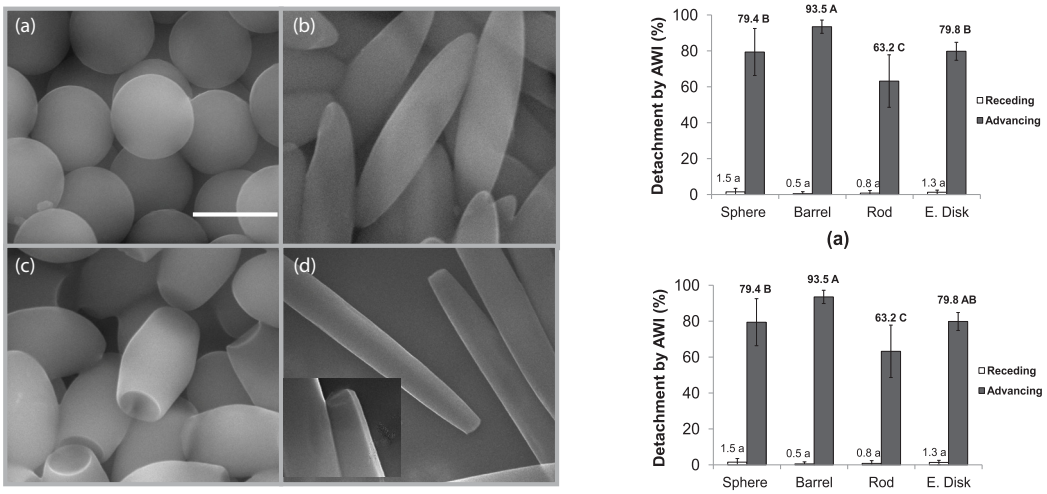


Figure 4. SEM images of four selected shapes of colloids: (a) sphere, (b) rod, (c) barrel, and (d) elliptical disk. (Scale bars: 1 $\mu$m) (left) and percentage detachment of deposited colloids as function of shapes by AWI: Different letter indicating statistical difference determined by (a) LSD and (b) Tukey's at the 95% confidence level (right).

away from the Columbia River between the 200E and 200W areas of the Hanford Reservation. We selected particles with typical mineralogy for the Hanford sediments: basalt, granite, hematite, magnetite, mica, milky quartz, and clear quartz. Standard-shaped model particles were used to delineate the dependency of the measured forces on particle shape. Particles were characterized for air-water contact angles, shape, and surface roughness. The particle outlines in the $xy$- and $xz$-planes were determined by scanning electron microscopy and used to quantify the dimensions along the three coordinate axes. The capillary forces between the particles and the air-water interface were measured with a tensiometer (Figure 5). We determined the forces as a function of position of the air-water interface at the particle. Force measurements were made for "as is" particles, i.e., as collected from the field, as well as for particles washed and treated to remove soluble organic surface coatings.

Theory was developed to calculate capillary forces for non-spherical, irregularly-shaped particles. The theory available for spherical particles was expanded to ellipsoidal particles and is based on a force balance approach:

$$f = f_{\mathrm{DLVO}} + f_{\mathrm{w}} + f_s + f_b + f_p \tag{1}$$

where the terms are the DLVO force ($f_{\mathrm{DLVO}}$), the gravity force ($f_{\mathrm{w}}$), the surface tension force ($f_s$), the buoyancy force ($f_b$), and the hydrostatic pressure force ($f_p$). If the particle is

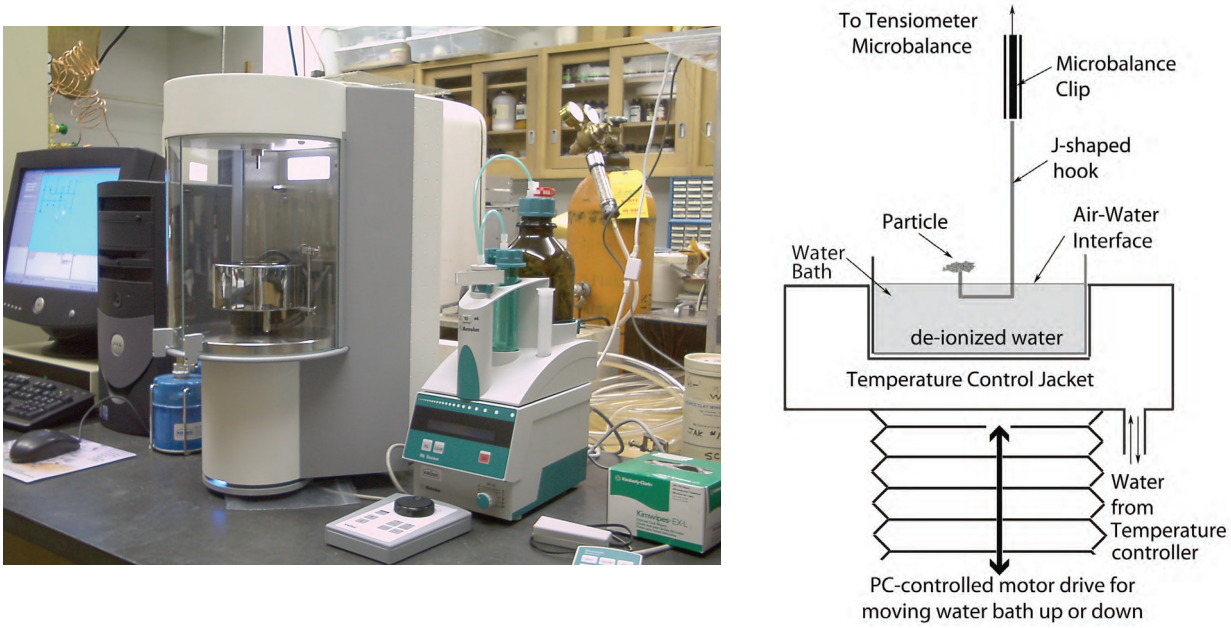


Figure 5. Process tensiometer and schematic of capillary force measurements for natural subsurface particles.

symmetric, the force balance $f$ is parallel to the $z$-direction (Figure 6a), but if the particle is asymmetric, the directions of $f_s$ and $f_p$ forces are determined by the contact angle of the air-water interface at the particle surface. Further, for asymmetric particles, the interface line is undulating in quadrupolar fashion. If $f < 0$ the particle will be detached from the solid surface, if $f > 0$ the particle will remain pinned to the solid surface.

We further developed the theory for a spherical particle to a triaxial ellipsoid. Theoretical calculations of capillary forces on ellipsoidal particles showed that the contact line is of an undulating, elliptic shape rather than a flat ellipse. The force balance on an ellipsoidal particle is then given as:

$$f = 4a\kappa E(e_{xy})\gamma \cos\beta \sin\phi_c + \pi ab\Delta\rho g z_c \cos^2\beta - \frac{\pi}{3}\Delta\rho g abc(2 + 3\sin\beta - \sin^3\beta) \qquad (2)$$

where $a$, $b$, and $c$ are the semi-principal axes of the ellipsoid along the three coordinate axes $x$, $y$, and $z$, respectively, $\kappa$ is the ratio representing increase in contact line due to undulation, $E(e_{xy})$ is the complete elliptic integral of the second kind with eccentricity $e_{xy}$, $\beta$ is the parametric latitude, $\gamma$ is the surface tension of water, $\phi_c$ is the angle of inclination of the undistorted air-water interface at the three-phase contact line, $\Delta\rho = (\rho_l - \rho_g)$ is the difference between the two fluid densities $\rho_l$ (water) and $\rho_g$ (air), $g$ is the acceleration due to gravity, and $z_c$ is the deflection depth (position of the average contact line on the $z$-axis).

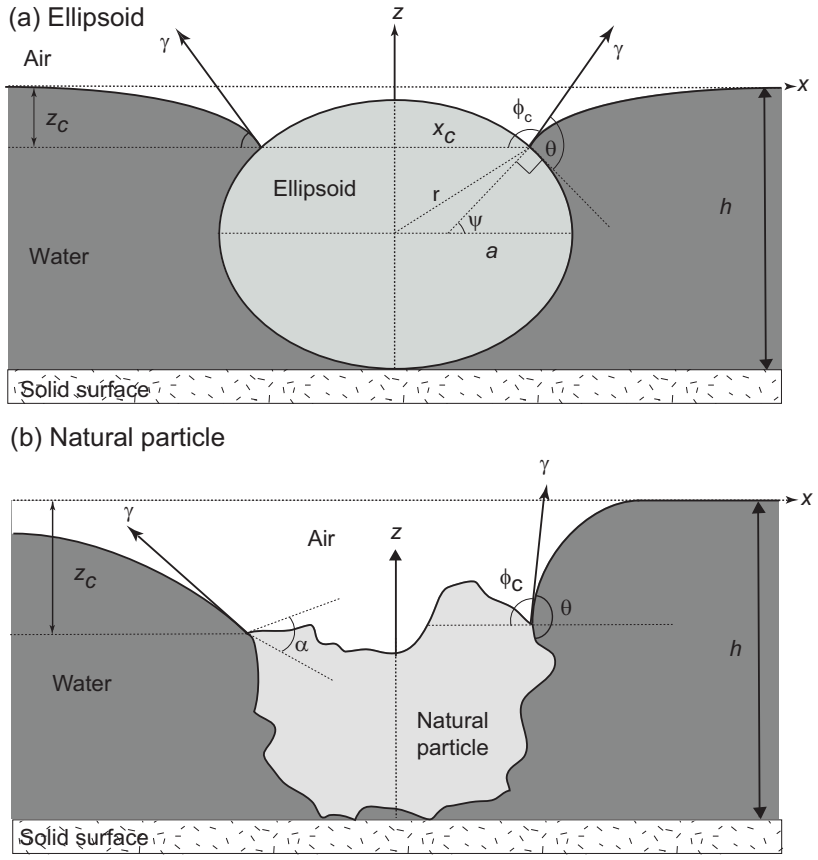


Figure 6. Forces acting (a) on a smooth, ellipsoidal particle with semi-principal radii $a$, $b$, $c$, and (b) on an asymmetric, rough particle in contact with an air-water interface, where $\psi = (\frac{3\pi}{2} - \theta - \phi_c)$ and $\alpha$ is the wedge angle for a sharp point on a surface where pinning occurs.

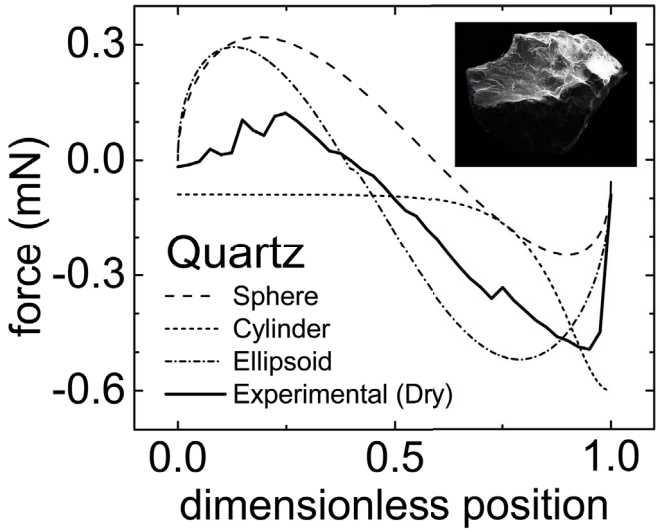


Figure 7. Force-position curves of sphere, circular cylinder, and ellipsoid (theoretical) and a dry, uncleaned quartz particle (experimental) during immersion.

**3.4.2.3 Principal Results** Figure 7 shows the dimensionless force-position curves for the dry PTFE particles of standard shapes and for the quartz particle. We use quartz as example here to illustrate the behavior of a natural sediment particle. The shape of the curves for the standard particles are related to their geometries. The curves for the PTFE sphere and disk are symmetrical with the immersion and emersion curves almost exact mirror images. Both particles show a large snap-off force, with the disc showing the most pronounced snap-off effect due to interface pinning. The tent and the quartz particle also show snap-off force, due to interface pinning. However, during emersion, there was no snap-in for both the tent and the quartz particle, as the interacting surface area of the particle with the air-water interface is small.

For the natural particles, the snap-off forces are, in general, smaller than the maximum capillary forces, but in some cases the snap-off force equals the maximum force. This occurs when the air-water interface is pinned at the particle surface strong enough so that snap-off happens under conditions represented by the Gibbs extension of the Young Equation. The more pronounced the pinning, the more likely the air-water interface snaps off at the maximum capillary force.

Theoretical and experimental values of capillary forces were of similar order of magnitude. The sphere gave the smallest theoretical capillary force, and the circular cylinder had the largest force due to pinning of the air-water interface. Pinning was less pronounced for natural particles when compared to the circular cylinder. Ellipsoids gave the best agreement with measured forces, suggesting that this shape can provide a reasonable estimation

of capillary forces for many natural particles.

### *3.4.3 Interaction between Hanford Colloid and Humic Acids*

**3.4.3.1 Materials and Methods** Colloids (operationally defined in this work as particles with diameters less than 2 $\mu$m) were isolated from fine Hanford sediments representative of those found underneath the Hanford radioactive waste tank farms. An aliquot of the prepared colloid stock solution was treated with 30% vol/vol $H_2O_2$ to serve as an OM-free control suspension. Total metal e.g., Al, Ca, Fe, Mg, Mn (microwave-assisted HNO3/HF digestion followed by ICP-OES), C and N (C/N analyser) concentrations were determined for the isolated colloids. Sorption isotherm experiments were carried out using Suwannee River FA and Aldrich HA standard materials. Sorption experiment solutions (pH 7, 1 mM $CaCl_2$ background) with colloid concentrations of 1 g $L^{-1}$ and FA or HA concentrations ranging from 0 to48 mg $L^{-1}$ were used. No-colloid control solutions were also used. Sorption experiment suspensions were equilibrated on a shaker (17 hours, room temperature) and aliquots of reacted suspensions were used for characterization. Colloids were then centrifuged out of solution and metal (ICP-OES), C and N (TOC analyzer) concentrations in the equilibrium aqueous phases were determined. Natural, FA/HA-reacted and H2O2-treated colloids were characterized using FTIR spectroscopy and SEM-EDAX. Changes in colloid particle size (at pH 7 and 1 mM $CaCl_2$) and electrophoretic mobility at different values of pH (4, 5, 7, 8, 9, 10) and sorption experiment solution ionic strength (0.01, 0.1 and 1 mM $CaCl_2$) were measured using dynamic light scattering.

**3.4.3.2 Principal Results** Results from this investigation indicated that the maximum sorption capacity of Suwannee River FA on Hanford colloids was about 4 mg C/g and a Langmuir type adsorption isotherm shape was observed, suggesting monolayer sorption of FAs on these colloids. At pH 7 and 1 mM $CaCl_2$ ionic strength, no differences in particle size were observed between the natural colloids and FA-reacted colloids but a greater particle size was found for the $H_2O_2$-treated colloids, suggesting aggregation of particles in absence of organic matter coatings. Also, under these conditions, the natural and FA-reacted colloids had more negative electrophoretic mobility values than the $H_2O_2$-treated colloids. Furthermore, electrophoretic mobility values for the FA-reacted colloids generally became increasingly negative with increasing FA reaction concentration. These findings suggest that OM stabilizes the Hanford colloids. Results from this investigation of the interactions between Hanford colloids and HS indicate that natural OM and HS do have a stabilizing effect on colloids from the Hanford radioactive waste repository. The impact of these findings is that OM has the potential to increase the reactivity of Hanford colloids towards contaminants and ultimately influence their participation in colloid-facilitated contaminant transport.

## 3.5 Column-Scale Investigations on Transport in Unsaturated Hanford Sediments and Porous Media

### *3.5.1 Using a Geocentrifuge to Elucidate Effects of Flow Rates and Water Content on Colloid Transport and Mobilization*

(*References:* Knappenberger et al., 2012)

**3.5.1.1 Motivation** Water content and flow rate play an important role in colloid mobilization in unsaturated porous media. It is important to determine the role and the interplay of these factors to obtain a mechanistic understanding of the colloid mobilization process. Unfortunately, under normal gravity, water content and flow rate cannot be independently controlled (the relationship between water content and hydraulic conductivity is hysteretic, but we do not have experimental control over hysteresis). Only with geocentrifuges we can vary each factor independently.

**3.5.1.2 Materials and Methods** In unsaturated porous media water flow is described by the Darcy-Buckingham-law:

$$q_w = -K(\psi_m)\left(\frac{\partial \psi_m}{\partial z} + 1\right) \tag{3}$$

where $q_w$ is the flux density, $K(\psi_m)$ is the unsaturated hydraulic conductivity and $\psi_m$ is the matric potential of the media. After Eqn. 3 the water flow is a function of the unsaturated hydraulic conductivity and the gradient of matric and gravimetric potential. The gradient of the gravimetric potential is 1 under gravity. If an unsaturated water flow is developed in a centrifugal field, Eqn. 3 can be rewritten as:

$$q_w = -K(\psi_m)\left(\frac{\partial \psi_m}{\partial r} - \rho\omega^2 r\right) \tag{4}$$

where $\rho$ is the density of the liquid, $\omega$ is the angular speed, and $r$ is the radius from the center of rotation. In a centrifugal field it is possible to realize different flux densities $q_w$ at constant matric potentials $\psi_m$ and hence constant water contents by varying the angular speed. Or, a flux density can be realized at different matric potentials $\psi_m$ and water contents, respectively. Consequently, in a centrifugal field, it is possible to overcome the limitations of the Darcy-Buckingham-law of only realizing a certain flux density at a certain water content. In terms of colloidal research, this means that effects of water content and pore water velocity can be considered independently by performing unsaturated flow experiments in a centrifugal field.

**Column Setup:** We used a plexiglass column with an inner diameter of 5.08 cm and a

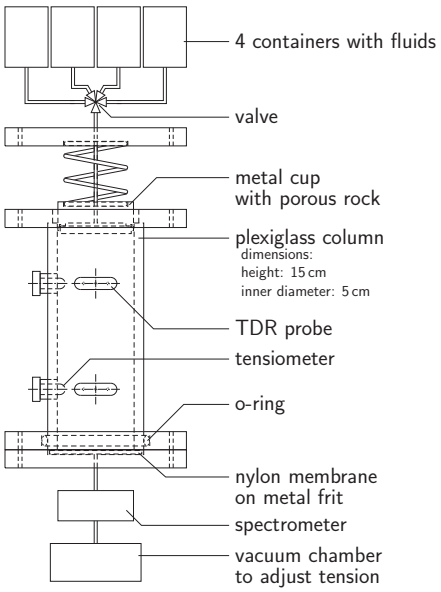


Figure 8. Column setup and principal arrangement of data acquisition devices.

length of 15 cm (Figure 8). At the bottom we used a nylon membrane, mesh size 500 on top of a metal frit. The suction was applied with a vacuum pump via a vacuum chamber. The applied suction on the bottom of the column was controlled with a pressure sensor under the metal frit. In a distance of 4 and 11 cm from the bottom we installed tensiometers and TDR probes to measure the water potential and the water content. The suction on the tensiometers was measured with pressure sensors. The reflection curve on the TDR probes was measured with a Tektronixs cable tester and logged with a data logger. We designed the TDR probes to fit the column and used state-of-the-art 3D printing techniques to produce the probes. The liquids were introduced into the column through a porous stone to ensure an even distribution over the whole cross-sectional area of the column.

**Porous Media:** We used Baker silica sand as a porous medium. The sand was pretreated with 2 M HCl at 90 °C temperature for 24 h to remove organic components and has a porosity of $\epsilon = 0.377$ and a bulk density of $\rho_b = 1.65\,\mathrm{g/cm^3}$. The saturated pore volume ($\mathsf{pv_s}$) in the column is $114.62\,\mathrm{cm^3}$.

**Model Colloids:** We used two kinds of carboxylate modified polystyrene colloids with a diameter of 26 and 220 nm. We used a concentration of $2.5 \cdot 10^{15}$ particles/L for the 26 nm colloids and a concentration of $10^{12}$ particles/L for the 220 nm colloids.

**Nitrate Tracer and Solution Chemistry:** A 0.2 M $NaNO_3$ solution was used as a tracer to evaluate the unsaturated flow conditions. We applied the $NaNO_3$ prior to the colloid experiments to check for uniformity of the flow conditions between single experiments. The solution chemistry was changed during our experiments to vary colloid attachment

Table 2. Sequence of liquids applied in colloid experiments.

| Phase | Pore Volumes | Description |
|---|---|---|
| A | 2 | nano pure water |
| B | 4 | 0.2 mM $NaNO_3$ |
| C | 2 | nano pure water |
| D | 2 | 1.67 mM $NaHCO_3$ , 1.67 mM $Na_2CO_3$, 100 mMol NaCl |
| E | 7 | 1.67 mM $NaHCO_3$ , 1.67 mM $Na_2CO_3$, 100 mMol NaCl, colloids |
| F | 5 | 1.67 mM $NaHCO_3$ , 1.67 mM $Na_2CO_3$, 100 mMol NaCl |
| G | 10 | nano pure water |

conditions. We used a total of three different solutions for colloid transport: nano pure water (liquid I), nano pure water with high ionic strength (liquid II), and nano pure water with high ionic strength and colloids (liquid III). Nano pure water with an electrical conductivity of less than $5.5 \cdot 10^{-6}\,\mathrm{S\,m^{-1}}$ acted as a starting liquid (liquid I). We buffered nano pure water at pH 10 (1.67 mM $NaHCO_3$ and 1.67 mM $Na_2CO_3$) and added 100 mM NaCl to increase the ionic strength to 106 mMol (liquid II). The stock of liquid II was split and colloids were added to one part (liquid III).

**Sequence of Liquids:** We introduced nano pure water at the beginning of the experiments and developed a steady state flow. After reaching a steady state flow, we introduced the different liquids in a certain sequence for the two different colloids. Every sequence was repeated three times. First we introduced three sequences of the 220 nm colloids and subsequently we introduced three sequences of the 26 nm colloids. We applied the $NaNO_3$ prior to the colloid experiments. The sequences of liquids are shown in Table 2.

**Experiments Under Gravity and Centrifugal Force:** The silica sand was introduced into the water filled column to ensure saturated conditions. The liquids were introduced to the column with a peristaltic pump. After a series of 220 nm and 26 nm colloids experiments, we removed the sand from the column, sonicated and washed it with deionized water. For the experiments under centrifugation we used the geocentrifuge facility at the Idaho National Laboratory (50 g-tonne Actidyn Systemes model C61-3, France). The experimental platform has a size of 70 cm length by 50 cm depth by 60 cm height. The radius of centrifugation is 2 m. The geocentrifuge accepts a pay load of 500 kg and accelerations up to 130 g. The centrifuge experiments were the same as the experiments under gravity but we used a piston pump to introduce the liquids into the column. First, we acquired a calibration curve by setting the centrifuge to different accelerations (2 g, 10 g, 20 g, 30 g and 40 g) and applying different flow rates. Then we calculated the corresponding pore water velocities according to different accelerations (Figure 9). Based on these measurements we designed the experiments accordingly.

**Spectrophotometry:** We used a spectrophotometer to measure the colloid concentra-

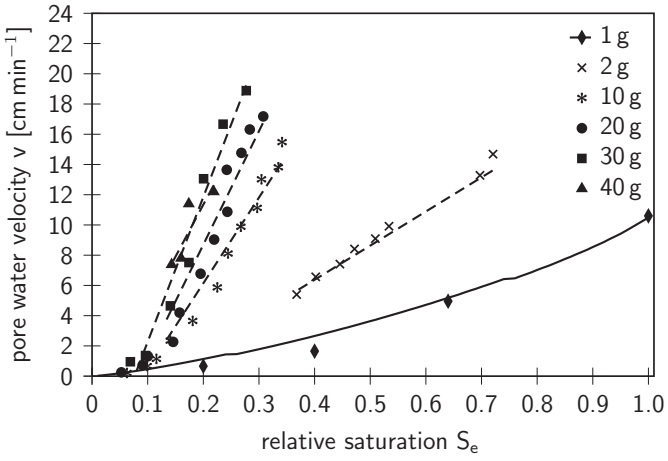


Figure 9. Different pore water velocities over effective saturation ($S_e$) at different accelerations. The solid line in the 1 g case was calculated based on van Genuchten parameters.

tions in the outflow of the column. Solarization resistant fiber optics were used (QP400-2-SR) to connect the light source to the spectrophotometer. We measured the concentrations of all liquids before every experimental series by injecting the liquid into the flow cell.

**3.5.1.3 Principal Results** Figure 10 shows the breakthrough and release curves for the 26 and 220 nm colloids and for effective saturations of 0.2, 0.3, 0.6 and 1. Overall, the breakthrough curves decrease with decreasing effective saturation. The first breakthrough curve of a series of three experiments is less pronounced than the second and third breakthrough curve. In case of the 26 nm colloids and an effective saturation of $S_e = 0.3$, no breakthrough occurred for the first run of the series (Figure 10E). The release curves for 220 nm colloids under saturation were very pronounced and reached values of 3.8, 2.2 and 2.3 $C/C_0$ for run 1, 2 and 3, respectively. Figure 11 shows the mass balance for the 26 and 220 nm colloids. Overall, larger amounts of 26 nm colloids are retained.

The runs within a series of experiments as well as the effective saturation levels had highly significant effect. Even release curves, whose shape was apparently alike (e.g., Figure 10A, 10C, 10D) had highly significant differences. The adjusted $R^2$-values were 0.61 and 0.69 for breakthrough and release curves for 26 nm colloids and 0.82 and 0.39 for breakthrough and release curves for 220 nm colloids, respectively.

Under saturated conditions ($S_e = 1$), introduced colloids can attach to primary and secondary energy minima. That means an introduced colloid can either pass the column without attachment or the colloid can attach to a primary or secondary energy minimum. If attached to a secondary energy minimum, the particle will be released again after changing

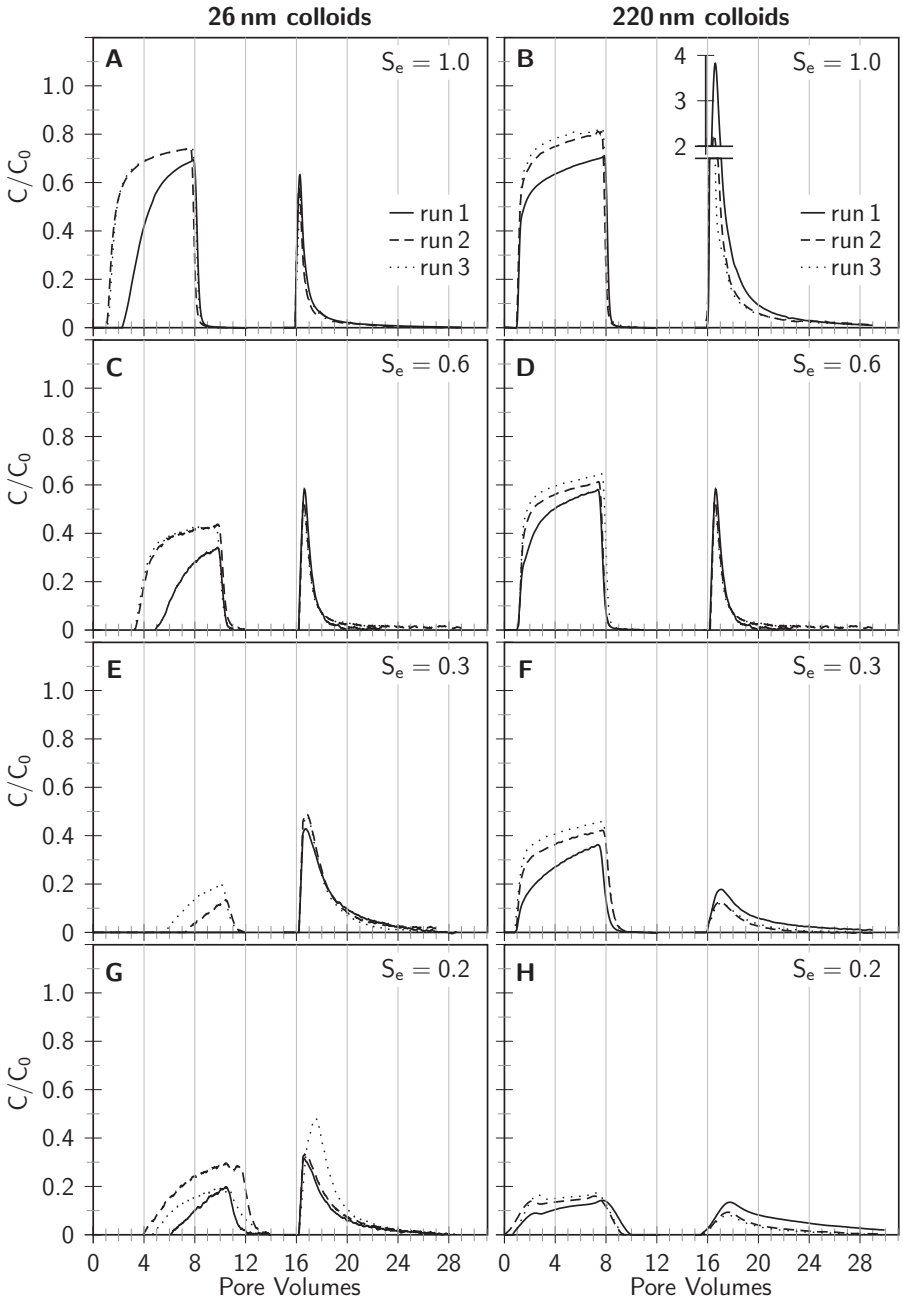


Figure 10. Overview of all breakthrough and release curves.

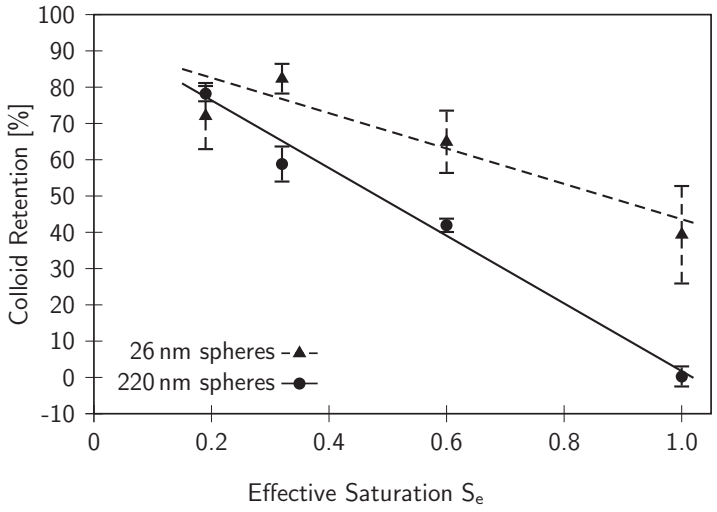


Figure 11. Colloid retention mass balance in geocentrifuge experiments.

the solution chemistry (change from phase F to G, Table 2). Consequently the secondary energy minimum will vanish and the retained colloids will be released (Figure 10). For 220 nm colloids, all colloids were leached out, i.e., colloids have only been retained in a secondary energy minimum. However, 23% of 26 nm colloids remain retained in the column. That means colloids also have to be retained in a primary energy minimum as no other attachment sites are available.

Under unsaturated conditions ($S_e < 1$), besides the mentioned primary and secondary energy minima, colloids can also attach to the liquid-gas-interface. With decreasing water content, the liquid-gas-interface is increasing and hence more attachment sites for colloids become available. For both colloid sizes, the retention increases with decreasing effective saturation (Figure 11). We assume that more colloids are retained at the liquid-gas-interface as the effective saturation is decreasing.

More detailed mass balance data are listed in Table 3. For the 26 nm colloids, the series at an effective saturation of $S_e = 0.3$ does not fit into the overall pattern. In the other series, the percentages for the breakthrough curves increase with increasing saturation from 15.9 % at $S_e = 0.2$ to 55.2 % at $S_e = 1$. With less saturation, less colloids pass the column after introduction. We attribute this effect to a larger liquid-gas interface. The colloids find more attachment sites at this interface. The percentage of released colloids, however, is constant for $S_e = 0.2$ and $S_e = 0.3$ as well as $S_e = 0.6$ and $S_e = 1.0$. The Kruskal-Wallis test for breakthrough, release and retention is significant at $p = 0.023$, $p = 0.036$ and $p = 0.033$, respectively.

For the 220 nm colloids, the percentages for the breakthrough curves increase with

Table 3. Mass balance for breakthrough and release curves and overall retention (in percent). Mean values and standard deviations are listed in this table. The p-values are computed with a Kruskal-Wallis test over all effective saturation values.

| | effective Saturation $S_e$ | | | | |
|---|---|---|---|---|---|
| | 0.2 | 0.3 | 0.6 | 1.0 | p-value |
| | 26 nm colloids | | | | |
| Breakthrough | 15.9 ± 8.0 | 4.5 ± 4.6 | 29.1 ±10.6 | 55.2± 14.8 | 0.023 |
| Release | 12.1 ± 5.1 | 13.2 ± 2.4 | 5.9 ± 1.8 | 5.4 ± 1.1 | 0.036 |
| Retention | 72.0 ± 9.4 | 82.3 ± 4.4 | 65.0 ± 8.9 | 39.3 ±13.7 | 0.033 |
| | 220 nm colloids | | | | |
| Breakthrough | 14.3 ± 1.6 | 34.7 ± 7.3 | 51.4 ± 5.6 | 70.6 ± 6.4 | 0.016 |
| Release | 7.5 ± 4.0 | 6.5 ± 2.6 | 6.6 ± 3.7 | 29.1 ± 9.3 | 0.092 |
| Retention | 78.2 ± 2.4 | 58.8 ± 5.1 | 41.9 ± 2.1 | 0.3 ± 3.1 | 0.016 |

increasing saturation from 14.3 % at $S_e = 0.2$ to 70.6 % at $S_e = 1$. The percentage of for the release curve is constant for unsaturated conditions and is significant higher for saturated conditions. The missing liquid-gas interface in the saturated condition obviously allows more colloids to be trapped in the secondary energy minimum. Under unsaturated conditions, the liquid-gas interface is available as attachment site and the number of colloids that are trapped in the secondary energy minimum is smaller but constant. The differences are not significant $p = 0.092$. If only the unsaturated conditions are considered in the Kruskal-Wallis test, the p-value even increases to $p = 0.837$.

Overall, the 220 nm colloids show a more consistent pattern and the mass balance data has a smaller standard deviation compared to the 26 nm colloids. However, we can determine attachments of 26 nm colloids to the solid-liquid interface in the primary energy minimum. We do not have evidence for such an attachment for the 220 nm colloids.

### *3.5.2 Colloid Mobilization in an Undisturbed Sediment Core under Semi-Arid Recharge Rates*

(*References:* Liu et al., 2012)

**3.5.2.1 Motivation** The Hanford site is characterized by a Mediterranean, semi-arid climate where deep recharge rates are low, ranging from near zero to 100 mm/y. It is unclear whether at these low, steady-state flow rates, colloids can be mobilized and transported. Here, we used an undisturbed sediment core to (1) test whether natural colloidal materials

can be mobilized and translocated under conditions typical for the deep vadose zone at the Hanford Site and (2) to quantify the extent of the colloid mobilization. We hypothesized that under the low and steady-state recharge rate at the semi-arid Hanford site, colloid mobilization and transport is low, but existent.

**3.5.2.2 Materials and Methods** An undisturbed sediment core was collected from the Hanford Environmental Restoration Disposal Facility (ERDF). The core was taken from an uncontaminated layer of the sand-dominated facies association of Hanford Formation sediments from a depth of 17 meters below ground surface (Figure 12a). A flat, horizontal bench of sediment was prepared by digging into the slanted wall of the ERDF pit. Then an intact, undisturbed core sample was taken by using a stainless steel cylinder (10 GA T-304, I.D. = 50 cm, height = 59.5 cm). A front-loader with a 3-m wide bucket was used to push the cylinder into the sediments (Figure 12b). When the core was completely inserted into the sediments, the sediments around the core were excavated, and a bevelled stainless steel plate was pushed along the bottom of the core to shave the core off the underlaying sediments (Figure 12c). About 17 liters of liquid nitrogen was poured onto the surface of the core to freeze the top of the core to provide stability for transportation. A wooden plate was tightened to the top of the cylinder, and the core was moved to Washington State University (Figure 12d).

The sediment core in the stainless steel column was set up as a lysimeter (Figure 12f) in a dark coldroom at $12.4 \pm 0.3$ $^o$C, corresponding to the long-term average air temperature at the Hanford site. The column was irrigated uniformly by using a peristaltic pump and a sprinkler. The irrigation rate was chosen to fall within the range of annual rainfall at the Hanford site. Based on the mass balance of the sediment core, we determined the actual infiltration rate to be 0.05 mm/day (= 18.25 mm/y), which corresponds to irrigation minus evaporation rates. This rate represents a low recharge rate typical for the Hanford site; rates have reported to range from 0 to 100 mm/y. Column outflow water was analyzed for particle size and electrophoretic mobility, pH, electrical conductivity, and UV/VIS absorbance at 280 nm. Absorbance was translated to particle concentrations by using a calibration curve developed from a colloid stock solution. Selected outflow samples were analyzed by transmission electron microscopy (TEM) and energy dispersive x-ray analysis (EDX).

We used HYDRUS-1D (Version 4.14) to analyze the water flow and colloid transport in our experiments. The unsaturated hydraulic properties were parameterized by the van Genuchten-Mualem equations. The model was run in inverse mode to determine the unsaturated hydraulic properties of the sediments. For the van Genuchten-Mualem model, we fitted the parameters $\alpha$, $n$, and $K_s$, with $m = 1 - 1/n$, for each of the observation nodes. For the colloid transport modeling, we assume that the pool of the colloids is initially uniformly distributed within the core and that the colloids are initially attached to

the stationary sediments. We further assume that, as water flows through the core, colloids can be mobilized by a first-order kinetic colloid release:

$$\frac{\partial C}{\partial t} + \frac{\rho}{\theta}\frac{\partial S}{\partial t} = D\frac{\partial^2 C}{\partial z^2} - \frac{J_w}{\theta}\frac{\partial C}{\partial z} \tag{5}$$

$$\frac{\partial S}{\partial t} = -\beta S \tag{6}$$

where $C$ represents the colloid concentration suspended in the aqueous phase (mg/cm$^3$), $S$ is the colloid concentration attached to the sediments (mg/g), $t$ is time (day), $\rho$ is the bulk density (g/cm$^3$), $z$ denotes the coordinate parallel to the flow direction (cm), and $\beta$ is the first-order colloid release rate coefficient (d$^{-1}$). A zero flux condition was used at the upper boundary ($J_w C(0,t) = 0$) and a zero-gradient was used at the bottom boundary ($\frac{\partial C}{\partial x} = 0$).

**3.5.2.3 Principal Results** Chemical and colloidal characteristics of the sediment outflow are shown in Figure 13. Electric conductivity varied between 500 and 2000 $\mu$S/cm, corresponding to ionic strengths of 7.2 to 29 mmol/L. The critical coagulation concentration for in situ colloids from Hanford sediments has been reported to be 1.7 to 3.8 mmol/L for Ca dominated systems. As the ionic strength in our core exceed the critical coagulation concentration, we did not expect any colloid dispersion to occur. The particle counts indeed indicate that colloid transport was not prominent in our sediment core. The initial outflow samples had particle counts below 10 kCounts/s, which is within the background noise of the dynamic light scattering instrument. No electrophoretic mobility and size measurements could be made for such low particle counts. In 2009, the particle counts increased up to 50 kCounts/s, which suggests the presence of particles in the outflow. Electrophoretic mobility and size measurements were made for these samples, but have to be considered with caution, as the particle counts still did not meet the required minimum value for accurate measurements (>50 kCounts/s). Electrophoretic mobility values, nonetheless, yielded reasonable results for Hanford sediments ($-1$ to $-3$ ($\mu$m/s)/(V/cm)). The particle concentration in the outflow ranged from generally 20 to occasionally 537 mg/L (Figure 13e), and we observed a continuous release of colloids (Figure 13f).

Figure 13f shows a continuous particle release from the sediment core at a rate of 148.1 mg/year. Over the total period of the experiment since colloid outflow was observed (967 days), a total of 0.392 g of particle were collected, corresponding to a cumulative particle flux of 0.2 mg/cm$^2$. The dispersible particles in the sediments was determined 84.1 g (0.441 g/kg sediments). The mobilized particles over 967 days constitute 0.5% (by mass) of the dispersible particles.

Model simulations could be fitted well to the experimental data (Figure 13f). The fitted colloid release coefficient was $\beta = 7 \times 10^{-6}$ day$^{-1}$, with lower and upper limit of 5.5

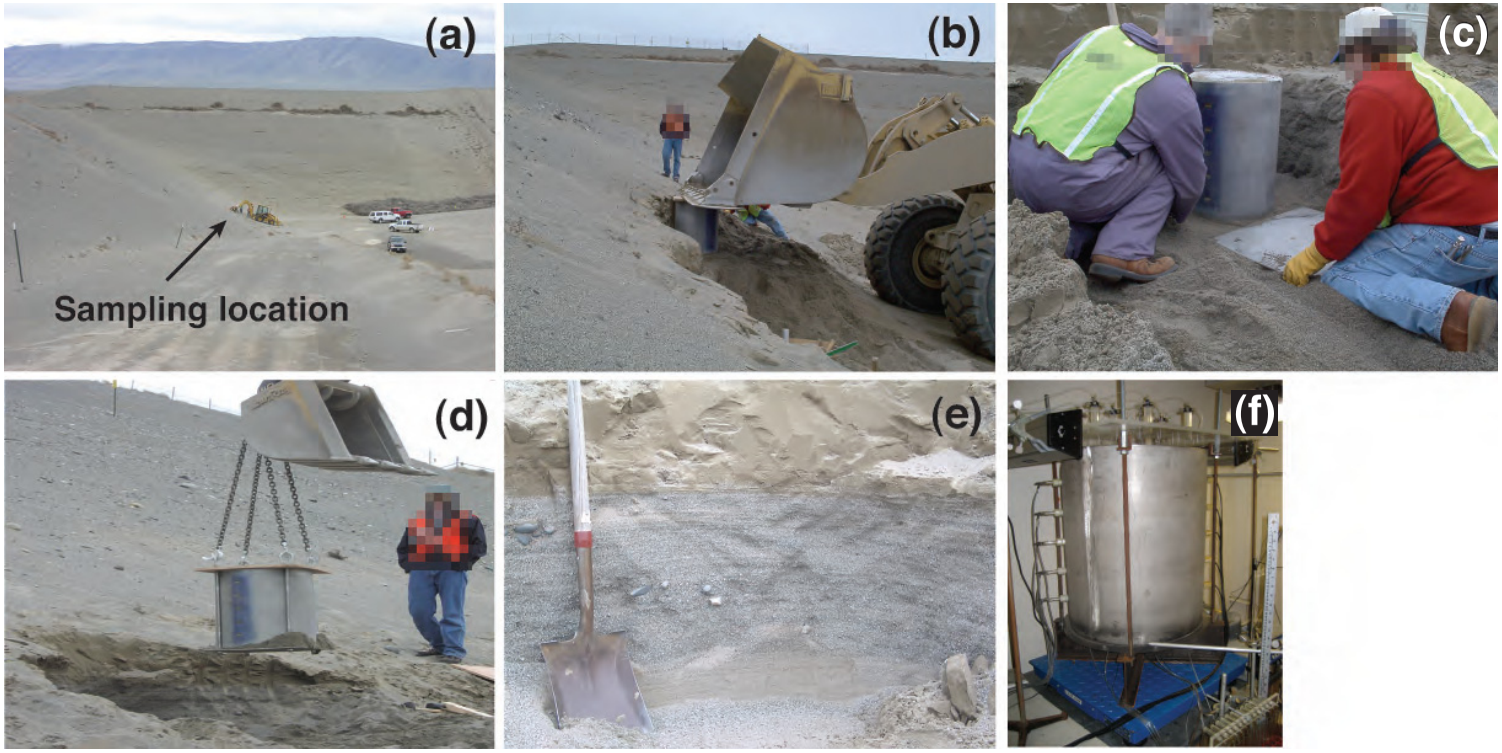


Figure 12. Sampling of sediment core and experimental setup. (a) Location of sampling in the ERDF pit, (b) insertion of steel cylinder into sediments, (c) shave-off of cylinder from sediments, (d) lift-off, (e) sediment layering of Hanford formation, and (f) laboratory setup.

and 9.5 $\times$ $10^{-6}$ day$^{-1}$, determined by adjusting the parameter $\beta$ to fully encompass the experimental data (Figure 13f). Using the same model with disturbed column experiments, we had previously found a range of colloid release rates from 10.1 day$^{-1}$ to 120 day$^{-1}$ for a flow rates from 259.2 mm/d to 414.7 mm/d. These values are six to seven orders of magnitude higher than the rate observed in the undisturbed sediments. This large difference in release rates indicates that particle release is considerably smaller in our undisturbed core under the much lower flow rate than in disturbed, packed columns at considerable high flow rates.

Our results suggest that even in semi-arid regions, the thick vadose zone with its low water content and flow rates does not necessarily constitute a perfect filter for particle transport. The continuous particle mobilization may constitute a pathway for contaminant and colloid-facilitated contaminant transport at the US DOE Hanford site.

## 3.6 Field-Scale Eu Colloid Transport at the Semi-Arid Hanford Site

### *3.6.1 Transport of Europium Colloids in Vadose Zone Lysimeters*

(*References:* Liu et al., 2012)

**3.6.1.1 Motivation** There exist no field experiments on colloid mobilization and transport at the Hanford Site. Several field lysimeter stations have been installed and operated at the Hanford site to study recharge, evapotranspiration, and mineral weathering. We used these these lysimeters to study colloid transport under field conditions.

**3.6.1.2 Materials and Methods** The study was conducted at the Hanford 300 Area Lysimeter site. The facility consists of six non-weighing lysimeters, each 7.6 m deep. Two of the lysimeters are 2.7 m in diameter and four lysimeters are 0.6 m in diameter (Figure 14). The 300 Area Lysimeters were installed in 1978 and all of them were kept free of vegetation for the past 34 years. These lysimeters were filled with a uniform sandy layer consisting of Hanford sediments and had a coarse sand layer at 5.7 m depth. The sandy layer's hydraulic conductivity is 173 cm/d at saturation and $9 \times 10^{-3}$ cm/d at $-5$ kPa. For our study, we used four lysimeters: the South Caisson (SC) and Lysimeters 1, 2, and 3 (Figure 14).

We installed fiberglass wicks to collect pore water samples from the lysimeters under unsaturated conditions. Fiberglass wicks have been found to be useful devices to collect pore water and soil colloids. The wicks were installed into the lysimeters in horizontal orientation at 0.31, 0.61, 1.22 and 2.14 m (1, 2, 4, and 7 feet). In Lysimeter 2, the wicks were installed at 0.61, 0.92, 1.22 and 2.14 m (2, 3, 4, and 7 feet) depths, because the access port at the 1-foot depth was inaccessible. A 50-cm long piece of the wicks was used as a hanging water column to provide tension for pore water sampling (Figure 15). This tension matches the water potential in the lysimeters and therefore provides little disturbance of the

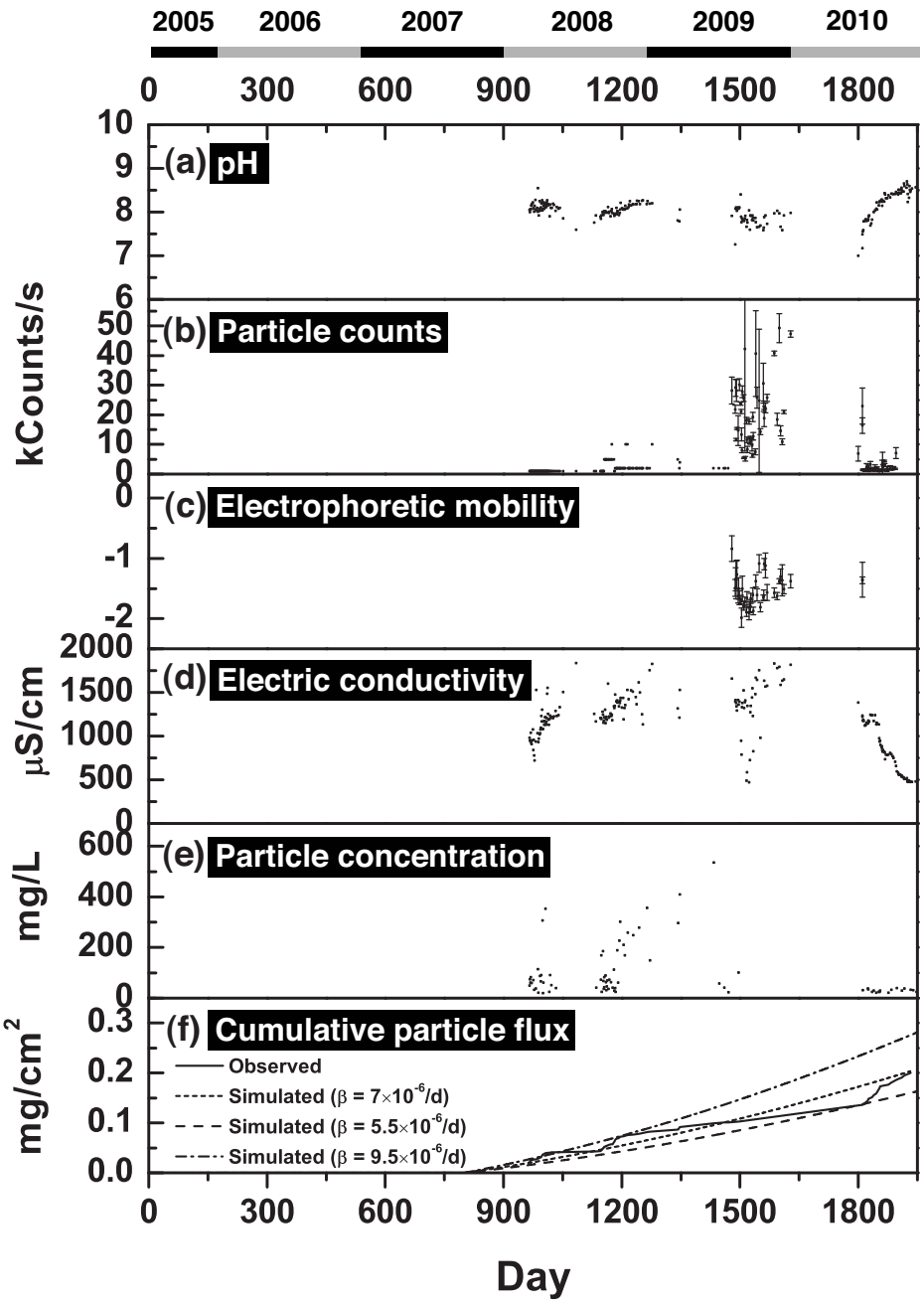


Figure 13. Characterization data of outflow from sediment core. (a) pH, (b) Particle counts, (c) Electrophoretic mobility (($\mu$m/s)(V/cm)). Unit is not shown in the figure due to space limit, (d) Electric conductivity, (e) Particle concentration, (f) Cumulative particle flux.

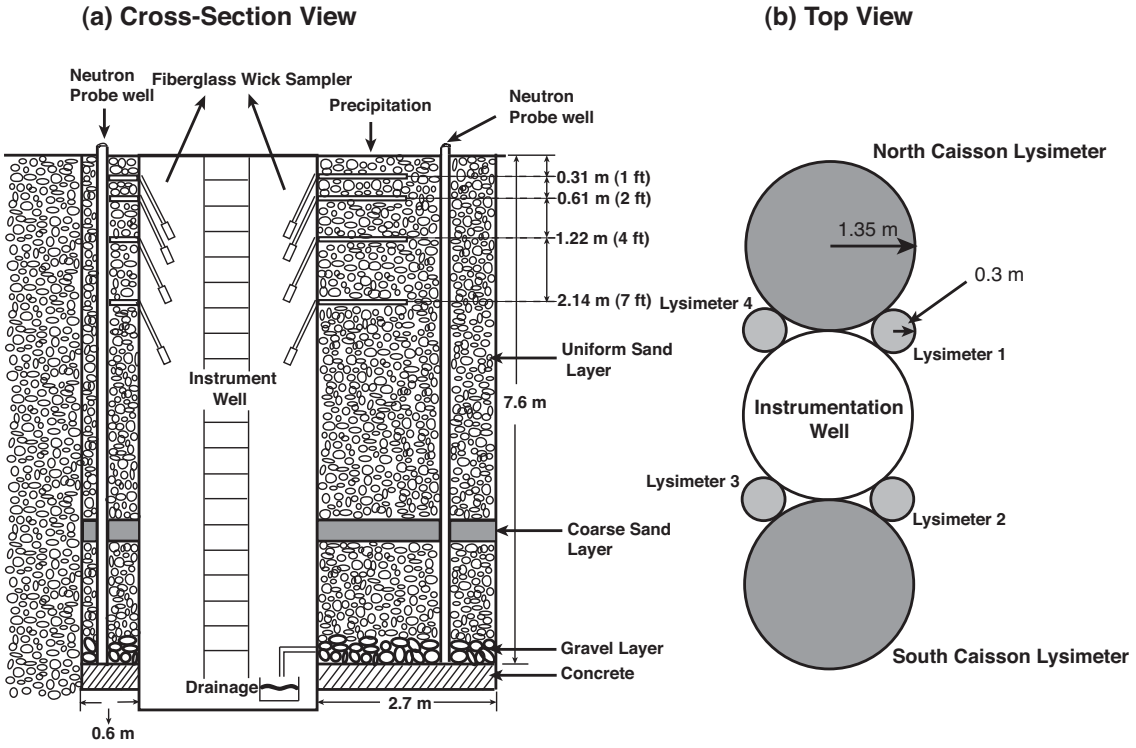


Figure 14. Schematic of Hanford 300 Area Lysimeter Facility. Only the South Caisson, Lysimeter 1, Lysimeter 2, and Lysimeter 3 were used in our experiments.

flow field. A 250 mL polypropylene bottle was placed at the bottom of each wick sampler to collect pore water.

Eu-hydroxy-carbonate colloids ($Eu(OH)(CO_3)$) were synthesized in our laboratory. A $6 \times 10^{-3}$ M europium stock solution was prepared by dissolving europium chloride ($EuCl_3 \cdot 5H_2O$) in double-distilled water, and then passed through a 0.2 $\mu$m filter. The filtered solution was mixed with 1.5 M urea and small amounts of acid ($7 \times 10^{-4}$ M $HNO_3$ and $2 \times 10^{-4}$ M $H_2SO_4$) in a 750 mL Pyrex bottle to adjust the pH to 5.1. The concentration of Eu colloids in this stock solution was 237.7 mg/L (measured gravimetrically by drying an aliquot), corresponding to a particle number concentration of $4.1 \times 10^{13}$ number/L (calculated based on average colloid diameter of 108 nm and specific density of 8.78 g/cm3). We used the Eu-hydroxy-carbonate colloids as a representative intrinsic radionuclide colloid.

A colloid suspension was then manually sprayed onto the lysimeter surface. A total of 3 mm of the suspension was applied to the lysimeters on March 11, 2009. Whereas the South Caisson Lysimeter was uncovered, receiving natural precipitation, and allowing evaporation, Lysimeters 1, 2, and 3 were irrigated and then covered to minimize evaporation. Lysimeter 1 received an annual recharge of 124 mm/year, which equals twice the 26-year drainage

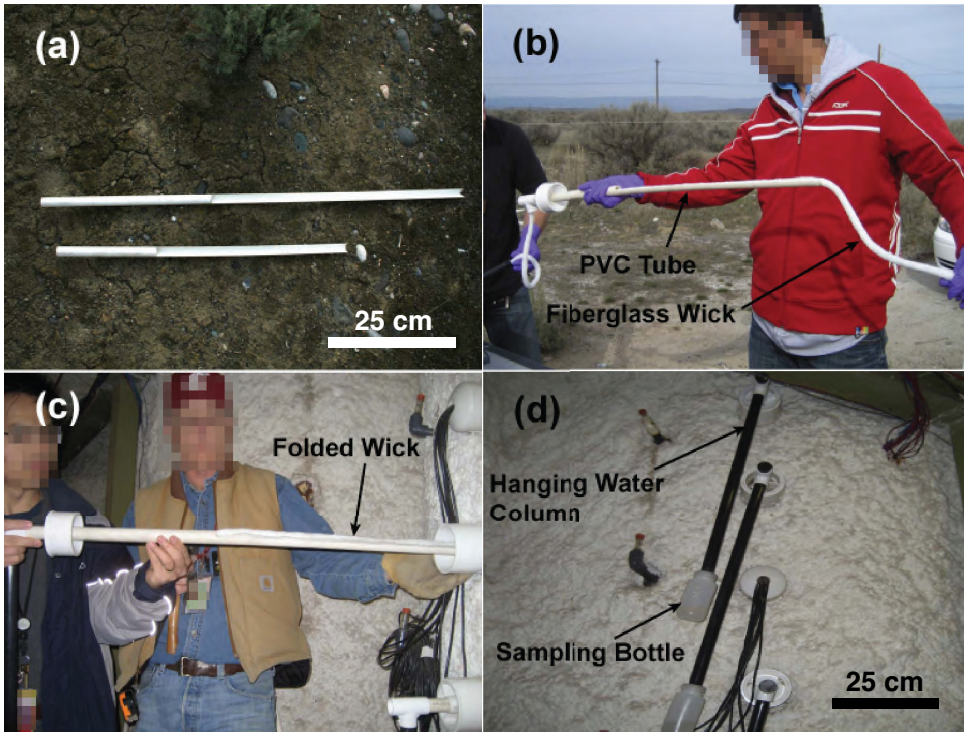


Figure 15. (a) Cut-open 3/4 inch PVC tube for wick support, (b) mounting of fiberglass wick (c) installation of wick sampler into lysimeter, (d) installed wick samplers showing the PVC tube containing hanging water column and the outflow sampling bottle.

average at the site. Lysimeter 2 was irrigated with four times the natural drainage, and Lysimeter 3 received an additional 100 mm/year simulated Chinook snowmelt event.

Outflow pore water from the fiberglass wicks was collected once a month by replacing the polypropylene bottles. Additionally, we took soil cores from the surface at different times. The collected pore water was first sonicated for 5 minutes and then analyzed for outflow volume, pH, electric conductivity, electrophoretic mobility, particle size, particle number, and particle mass concentration. Electrophoretic mobilities and particle counts were quantified by using dynamic light scattering, and repeated 5 times for each sample. Selected samples were examined microscopically using Transmission and Scanning Electron Microscopy, and Energy Dispersive X-ray analysis. The amount of Eu colloids was quantified by measuring the Eu concentration in the outflow samples or soil extracts.

**3.6.1.3 Principal Results** Figure 16a shows the daily natural precipitation and the irrigation from January 2009 to March 2012 for each of the lysimeters. The daily precipitation (South Caisson) was taken from the Hanford Meteorological Station and the irrigation (Lysimeters 1, 2, 3) was measured when it was applied. The natural precipitation occurred in much greater frequency than the irrigation, but the seasonal pattern was similar, not identical, because the irrigation was based on the long-term precipitation record. The Chinook events applied to Lysimeter 3 are indicated by arrows. In 2009, the Chinook simulation was applied at two separate days. The total application during a Chinook event exceeded 100 mm because the Chinook was added to the regular irrigation in that month.

While the Eu data for the South Caisson did not show a clear breakthrough pattern, we did detect Eu peaks in the irrigated lysimeters. Lysimeter 1 shows a Eu peak on June 29, 2009 at 1.22-m depth and on July 16, 2009 at 2.14-m depth. Similar patterns could be observed for Lysimeter 2 and 3. These initial peaks of Eu are corroborated by particle counts in the outflow samples (Figure 16d). Europium concentrations and particle counts declined during summer 2009 in most samples, because no outflow was collected, particularly for the top two wick samplers. The 2.14-m wick sampler showed continuous movement of Eu throughout the year in Lysimeters 1 and 2. A second peak of Eu could be detected in Spring 2010 in all lysimeters, caused by the elevated precipitation and irrigation during the preceding winter season. Particle counts, however, were not as pronounced as in 2009.

The Chinook events in Lysimeter 3 caused pronounced water infiltration and produced Eu peaks in the wick outflow, particularly in 2009. In 2010, the topmost wick (0.31 m) showed elevated Eu concentrations as a result of the Chinook event; correspondingly, there were increased particle counts in the wick outflow. The 0.61 m wick also showed elevated particle counts, however, no Eu was detected. The 2011 Chinook event, however, did not produce an Eu peak in the outflow.

The electrophoretic mobility data indicate that the wick outflow always contained par-

ticles, with electrophoretic mobilities between −0.5 to −3 ($\mu$m/s)/(V/cm). The pH of the wick outflow varied between 8.2 and 8.5. At that pH, the measured electrophoretic mobility of the water-dispersible, native colloidal fraction of the Lysimeter sediments (without Eu colloids) was −2.5 ($\mu$m/s)/(V/cm), and that of the Eu colloids (from the application suspension)) was −3.0 ($\mu$m/s)/(V/cm). This indicates that the outflow samples contained native colloidal material from the sediments. Figure 17 shows SEM images of wick outflow from May 28, 2009. The images reveal native colloidal materials (platy clay minerals, Figure 17a) as well as spherical particles (Figure 17b), which we identified as Eu colloids with the help of energy-dispersive x-ray analysis (Figure 18).

Our results demonstrate that under field conditions with transient flow, colloid mobilization and transport occurred in Hanford sediments. Small amounts of Eu colloids could be translocated by natural precipitation or irrigation to a depth of 2.14 m within 2.5 months. Assuming steady-state flow, this corresponds to a colloid transport velocity of 3 cm/d. Estimates of recharge at the Hanford site range from 1 to 50 mm/year. Considering a volumetric water content of 0.1 $m^3/m^3$, the recharge estimates translate to a pore water velocity of 1 to 50 cm/year (equal to 0.003 to 0.14 cm/d), which is considerably slower than what we observed based on the Eu transport. This indicates that the near surface transport of Eu can be rapid, exceeding recharged-based velocity estimates by more than a factor of ten. The measured maximal transport velocity of 3 cm/d, suggests that some of the Eu was transported by preferential flow.

The observed rapid movement of Eu in the homogeneous Hanford Lysimeters was caused by transient water flow near the soil surface. Based on the mechanistic laboratory studies reported above, it is likely that the Eu colloids were mobilized and translocated by moving air-water interfaces. The main peak of Eu, however, moved at slower rate, consistent with long-term recharge.

### *3.6.2 Field-Scale Conceptual and Numerical Model for Colloid Mobilization and Transport*

**3.6.2.1 Motivation** Mathematical models for colloid and colloid-facilitated transport are typically based on the advection-dispersion equation (ADE). For non-steady state flow, the ADE is usually coupled with the Richards equation describing water flow in variably-saturated porous media. The ADE for colloid-facilitated transport includes specific reactions of contaminants and colloids with the solid-water and the air-water interfaces. Alternatively, flow and transport can be modeled as two-phase flow (air-water), and a number of multiphase flow codes are available, for instance, FLOTRAN, NUFT, STOMP, and TOUGH2. These codes describe simultaneous flow of aqueous and gas phases under gravity, capillary, and viscous forces.

**3.6.2.2 Materials and Methods** The model PFLOTRAN was used to simulate colloid transport through the Hanford Vadose Zone at the 200 area. FLOTRAN is a reactive

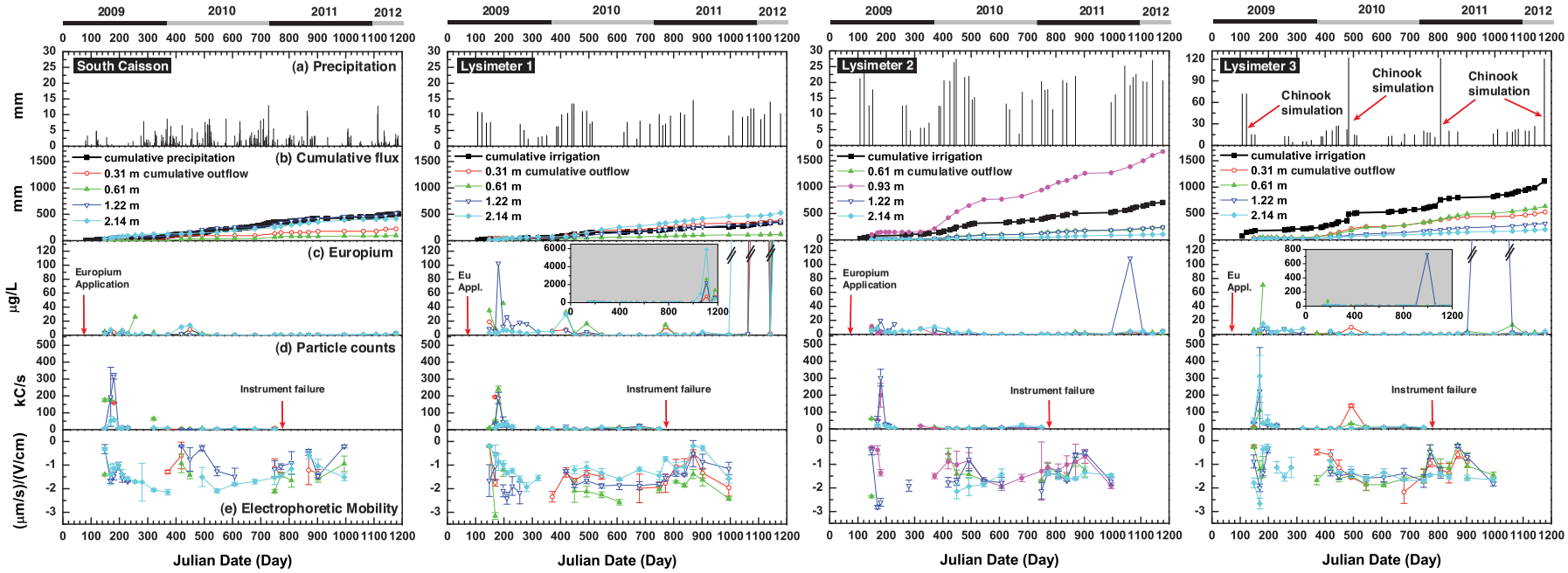


Figure 16. Time series of experimental data for each of the lysimeters. (a) Precipitation/irrigation, (b) cumulative water inflow on the surface and wick outflow, (c) Eu concentration in wick outflow (mass of Eu per volume of outflow solution); inserts show full-scale of Eu peaks observed in Fall/Winter 2011, (d) particle counts (kilocounts per s) in wick outflow , and (e) electrophoretic mobility of colloids in wick outflow.

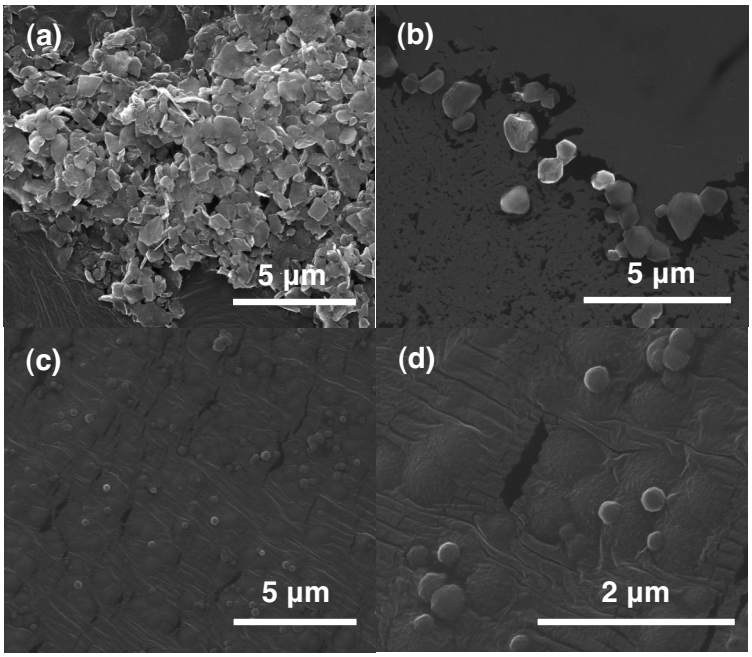


Figure 17. Scanning electron microscopy images of colloidal particles in wick outflow from different times.

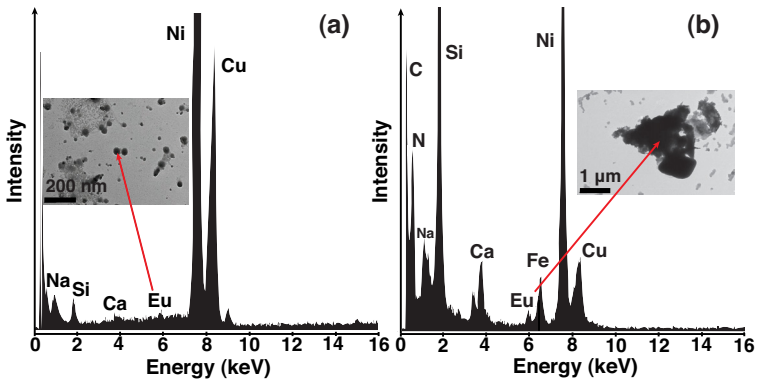


Figure 18. Energy dispersive x-ray spectra (EDX) and corresponding TEM images of wick outflow samples from (a) May 28, 2009, Lysimeter 1 (0.61-m depth), (b) June 18, 2009, Lysimeter 1 (0.31-m depth). The Eu L$\alpha$-level emission line at 5.8 keV indicates the presence of Eu. The large peaks for C, Ni, and Cu keV are from the microscopy stub.

flow and transport code that simulates two-phase (air and water) flow in variably saturated, nonisothermal porous media. Flow is governed by gravity, capillary, and viscous forces, and solves mass balance equations for water, air, and energy. The code handles multicomponent reactive chemical transport involving aqueous, gaseous, and mineral species. Chemical reactions include homogeneous aqueous speciation reactions, heterogeneous gaseous speciation, mineral precipitation and dissolution reactions, ion-exchange, and sorption reactions. The rates of mineral reactions are described through kinetic rate laws.

Colloid-facilitated transport is implemented in PFLOTRAN based on surface complexation reactions at the colloid surface. Competition between mobile and immobile colloids and stationary mineral surfaces is taken into account. Colloid filtration processes are not currently implemented into PFLOTRAN. A colloid is treated as a solid particle suspended in solution or attached to a mineral surface. Colloids may be generated through nucleation of minerals in solution, although this effect is not included currently in the code.

Three separate competing reactions may take place involving mobile and immobile colloids and mineral surfaces

$$>X_k^{\mathrm{m}} + \sum_j \nu_{jk}^{\mathrm{m}} \mathcal{A}_j \;\rightleftharpoons\; >S_k^{\mathrm{m}}, \tag{7a}$$

$$>X_k^{\mathrm{im}} + \sum_j \nu_{jk}^{\mathrm{im}} \mathcal{A}_j \;\rightleftharpoons\; >S_k^{\mathrm{im}}, \tag{7b}$$

$$>X_k^{s} + \sum_j \nu_{jk}^{s} \mathcal{A}_j \;\rightleftharpoons\; >S_k^{s}, \tag{7c}$$

for surface complexes $>S_k^{\mathrm{m}}$, $>S_k^{\mathrm{im}}$ and $>S_k^{s}$ and empty sorption sites $>X_k^{\mathrm{m}}$, $>X_k^{\mathrm{m}}$, $>X_k^{\mathrm{m}}$, where the superscripts $s$, $m$, and $im$ denote mineral surfaces, and mobile and immobile colloids, respectively. The species $\mathcal{A}_j$ form a set of primary species in terms of which all other reactions may be formulated. The corresponding reaction rates are denoted by $I_k^{\mathrm{m}}$, $I_k^{\mathrm{im}}$, and $I_k^{s}$, respectively. In addition, precipitation and dissolution reactions with minerals $\mathcal{M}_s$ may occur with reaction rate $I_s$ according to the reaction

$$\sum_j \nu_{js} \mathcal{A}_j \;\rightleftharpoons\; \mathcal{M}_s. \tag{8}$$

The transport equations for primary species based on Richards equation, mobile ($m$) and immobile colloids ($im$), read

$$\frac{\partial}{\partial t}\varphi s_l \Psi_j^l + \boldsymbol{\nabla}\cdot\boldsymbol{\Omega}_j^l \;=\; -\sum_k \left(\nu_{jk}^{\mathrm{m}} I_k^{\mathrm{m}} + \nu_{jk}^{\mathrm{im}} I_k^{\mathrm{im}} + \sum_s \nu_{jk}^{s} I_k^{s}\right) - \sum_s \nu_{js} I_s, \tag{9}$$

$$\frac{\partial}{\partial t}\varphi s_l S_k^{\mathrm{m}} + \boldsymbol{\nabla}\cdot\boldsymbol{q}_c S_k^{\mathrm{m}} \;=\; I_k^{\mathrm{m}}, \tag{10a}$$

$$\frac{\partial}{\partial t} S_k^{\mathrm{im}} \;=\; I_k^{\mathrm{im}}, \tag{10b}$$

$$\frac{\partial}{\partial t} S_k^{s} \;=\; I_k^{s}. \tag{10c}$$

In these equations $\boldsymbol{q}_c$ denotes the colloid Darcy velocity which may be greater than the fluid Darcy velocity $\boldsymbol{q}$ given by

$$\boldsymbol{q} \;=\; -\frac{kk_r}{\mu}\boldsymbol{\nabla}(p-\rho g z), \tag{11}$$

with permeability $k$, relative permeability $k_r$ a function of liquid saturation $s_l$, pressure $p$, fluid density and viscosity $\rho$, $\mu$, acceleration of gravity $g$, and porosity $\varphi$. The quantities $\Psi_j^l$ and $\boldsymbol{\Omega}_j^l$ refer to the total concentration and flux of the $j$th primary species defined, respectively, as

$$\Psi_j^l \;=\; C_j^l + \sum_i \nu_{ji} C_i^l, \tag{12}$$

and

$$\boldsymbol{\Omega}_j^l \;=\; \Big(\boldsymbol{q} - \varphi D\boldsymbol{\nabla}\Big)\Psi_j^l, \tag{13}$$

with diffusion/dispersion coefficient $D$. The total concentration and flux account for aqueous homogeneous reactions, assumed to obey conditions of local equilibrium, given by

$$\sum_j \nu_{ji}\mathcal{A}_j \;\rightleftharpoons\; \mathcal{A}_i. \tag{14}$$

The sorption reaction rates may be eliminated from the primary species transport equations and replaced by sorbed surface complex concentrations to yield

$$\frac{\partial}{\partial t}\Big[\varphi s_l \Psi_j^l + \sum_k \big(\varphi s_l \nu_{jk}^{\mathrm{m}} S_k^{\mathrm{m}} + \nu_{jk}^{\mathrm{im}} S_k^{\mathrm{im}} + \sum_s \nu_{jk}^{s} S_k^{s}\big)\Big] + \boldsymbol{\nabla}\cdot\Big(\boldsymbol{\Omega}_j^l + \boldsymbol{q}_c \sum_k \nu_{jk} S_k^{\mathrm{m}}\Big) \;=\; -\sum_s \nu_{js} I_s. \tag{15}$$

This result is obtained by substituting the left-hand sides of Eqns.(10a)–(10c) for the reaction rates. The mobile sorbed concentration appears in both the accumulation and flux terms, unlike the immobile and mineral sorbed concentrations. This is because of the flux term appearing in Eqn.(10a).

In the kinetic case either form of the primary species transport equations given by Eqn. (9) or (15) can be used provided it is coupled with the appropriate kinetic equations given by Eqns.(10a)–(10c).

The mobile case leads to additional equations that must be solved simultaneously with the primary species equations. A typical expression for $I_k^m$ might be

$$I_k^m \;=\; k_k\big(S_k^m - S_{km}^{\rm eq}\big), \tag{16}$$

with rate constant $k_k$ and where $S_{km}^{\rm eq}$ is a known function of the solute concentrations.

In this case, Eqn.(10a) must be added to the primary species transport equations. Further reduction of the transport equations for the case where a flux term is present in the kinetic equation is not possible in general for complex flux terms.

**Sorption Isotherm:** As follows from the mass action corresponding to the surface complex reaction the equilibrium sorption concentration $S_k^{\rm eq}$ is given by

$$S_k^{\rm eq} \;=\; \frac{\omega K_k Q_k}{1+\sum_l K_l Q_l}, \tag{17}$$

and the empty site concentration by

$$S_X^{\rm eq} \;=\; \frac{\omega}{1+\sum_l K_l Q_l}, \tag{18}$$

for selectivity coefficients $K_k$, and where the ion activity product $Q_k$ is defined by

$$Q_k \;=\; \prod_j \big(\gamma_j C_j\big)^{\nu_{jk}}. \tag{19}$$

The site concentration $\omega$ satisfies the relation

$$\omega \;=\; S_X + \sum_k S_k, \tag{20}$$

and is constant.

**Retardation:** Under the special circumstances of a sufficiently dilute solution so that the sorbed and aqueous concentrations can be treated as approximately constant, it is possible to define a retardation coefficient $\mathcal{R}_j$ as

$$\mathcal{R}_j \;=\; \frac{1+K_j^{\rm m}+K_j^{\rm im}+K_j^s}{1+f_c K_j^{\rm m}}, \tag{21}$$

where $f_c = |q_c/q| \geq 1$, and where the distribution coefficients $K_j^{\rm m}$, $K_j^{\rm im}$ and $K_j^s$ are defined

as

$$K_j^{\rm m} = \frac{1}{\Psi_j^l}\sum_k \nu_{jk}^{\rm m} S_k^{\rm m}, \tag{22a}$$

$$K_j^{\rm im} = \frac{1}{\varphi s_l \Psi_j^l}\sum_k \nu_{jk}^{\rm im} S_k^{\rm im}, \tag{22b}$$

$$K_j^{s} = \frac{1}{\varphi s_l \Psi_j^l}\sum_k \nu_{jk}^{s} S_k^{s}. \tag{22c}$$

With these definitions the solute transport equations ignoring diffusion/dispersion take the form

$$\frac{\partial \Psi_j^l}{\partial t} + \boldsymbol{\nabla}\cdot\left(\frac{\boldsymbol{v}}{\mathcal{R}_j}\right) = -\frac{1}{\mathcal{R}_j}\sum_s \nu_{js} I_s, \tag{23}$$

and is valid under the assumption that $\mathcal{R}_j \simeq$ constant.

Two limiting cases are of interest for Eqn.(21). In the absence of a mobile component ($K_j^{\rm m} \simeq 0$), then $\mathcal{R}_j$ reduces to the usual retardation coefficient based on sorption on stationary mineral and colloid surfaces

$$\mathcal{R}_j \simeq 1 + K_j^{\rm im} + K_j^{s} \geq 1. \tag{24}$$

If, on the other hand, the mobile component is dominant, $K_j^{\rm m} \gg K_j^{\rm im} + K_j^{s}$, then

$$\mathcal{R}_j \simeq \frac{1 + K_j^{\rm m}}{1 + f_c K_j^{\rm m}} \leq 1, \tag{25}$$

and the solute advances unretarded and possibly more rapidly than a non-reacting tracer.

**3.6.2.3 Principal Results** An example is presented in Figure 19 showing the effects of competition between sorption on a stationary mineral surface and mobile and immobile colloids for conditions of local equilibrium surface complexation reactions. The concentration profiles are compared to a non-sorbing tracer. A Darcy flow velocity of 1 m/y with a porosity of 0.5 in a fully saturated porous medium is considered. A total surface site density for colloids and mineral of 50 mol/dm$^3$ is used in the simulations with a colloid concentration of $10^{-7}$ mol/dm$^3$. A single surface complex for colloids and a mineral is used with the complexation reactions

$$>\!{\rm X} + {\rm A(aq)} \rightleftharpoons >\!{\rm XA}, \tag{26a}$$

$$>\!{\rm cX} + {\rm A(aq)} \rightleftharpoons >\!{\rm cXA}, \tag{26b}$$

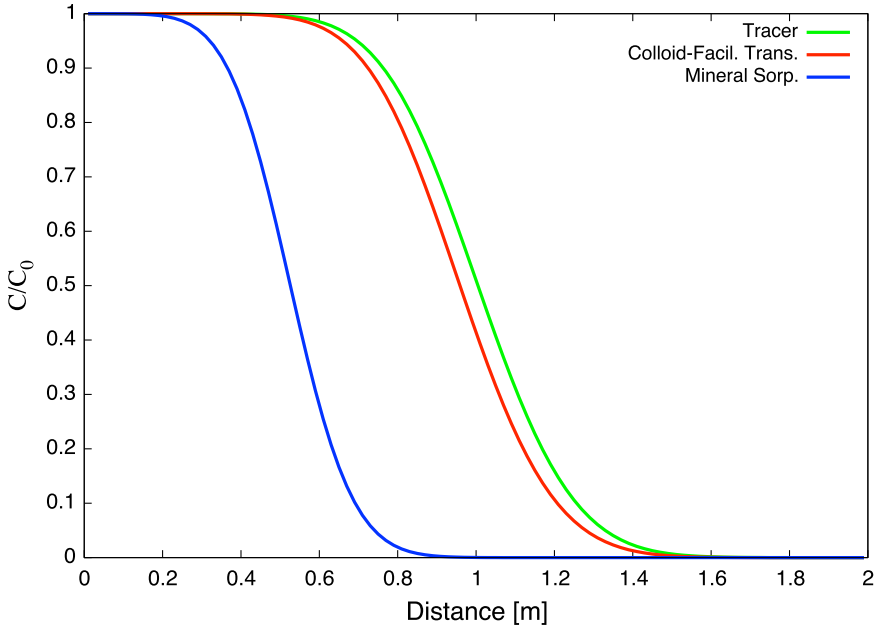


Figure 19. Normalized concentration plotted as a function of distance for a mineral sorbing solute (blue), non-sorbing tracer (green), and colloid-facilitated species transport (red).

with selectivity coefficients of $10^{-4}$. The species >cX and >cXA refer to colloids and >X and >XA to the mineral. The simulations are carried out for 0.5 y.

As can be seen from the figure, the mineral sorbing solute is the most retarded and retardation of the colloid-facilitated species is intermediate between no retardation and retardation by the stationary mineral surface.

# 4 Products Developed

## 4.1 Publications Published in Peer-Reviewed Journals (in inverse chronological order)

1. Chatterjee, N., S. Lapin, and M. Flury, Capillary forces between sediment particles and an air-water interface, *Environ. Sci. Technol.*, *46*, 4411–4418, 2012.

2. Aramrak, S., M. Flury, and J. B. Harsh, Detachment of deposited colloids by advancing and receding air-water interfaces, *Langmuir*, *21*, 9985–9993, 2011.

3. Shang, J., M. Flury, J. B. Harsh, and R. L. Zollars, Contact angles of aluminosilicate clays as affected by relative humidity and exchangeable cations, *Colloids Surf. Physicochem. Eng. Aspects*, *353*, 1–9, 2010.

4. Mattson, E. D., C. D. Palmer, R. W. Smith, and M. Flury, Centrifuge techniques and apparatus for transport experiments in porous media, in *Physical Modelling in Geotechnics*, edited by Springman, Laue, and Seward, pp. 1465–1470, Taylor and Francis Group, London, 2010.

5. Shang, J., M. Flury, and Y. Deng, Force measurements between particles and the air-water interface: Implications for particle mobilization in unsaturated porous media, *Water Resour. Res.*, *45*, W06420, doi:10.1029/2008WR007384, 2009.

6. Shang, J., M. Flury, J. B. Harsh, and R. L. Zollars, Comparison of different methods to measure contact angles of soil colloids, *J. Colloid Interface Sci.*, *328*, 299–307, 2008.

## 4.2 Unpublished Reports and Publications in Submission or Preparation

1. Liu, Z., M. Flury, Z. F. Zhang, J. B. Harsh, G. W. Gee, C. E. Strickland, R. E. Clayton, Transport of Europium Colloids in Vadose Zone Lysimeters at the Semi-Arid Hanford Site, submitted to *Environ. Sci. Technol.*, 2012.

2. Liu, Z., M. Flury, J. B. Harsh, J. B. Mathison, C. Vogs, Long-Term Water Flow and Colloid Transport in an Undisturbed Sediment Core at the Hanford Site, submitted to *Water Resources Research*, 2012.

3. Aramrak, S., M. Flury, J. B. Harsh, R. Zollars, H. P. Davis, Effects of Particle Shape on Colloid Detachment by a Moving Air-Water Interface. (in preparation, to be submitted to J. Colloid Interface Sci.), 2012.

4. Knappenberger, T., M. Flury, E. Mattson, J. B. Harsh, The Role of Flow Rate and Water Content in Colloid Transport in Unsaturated Porous Media. (in preparation, to be submitted to Environ. Sci. Technol.), 2012.

### 4.3 Presentations

1. Aramrak, S., M. Flury, J. B. Harsh, E. Mattson, H. P. Davis, Z. F. Zhang, G. W. Gee, P. Lichtner, Colloid Detachment by a Moving Air-Water Interface: Effect of Particle Shapes, Soil Science Society Annual Meeting Annual Meeting, Cincinnatti, Oct. 21-24, 2012.

2. Knappenberger, T., M. Flury, J. B. Harsh, E. Mattson, Using a Geocentrifuge to Study Colloid Transport in Unsaturated Porous Media, Karlsruhe Intitute of Technology, Karlsruhe, Germany, May 1, 2012.

3. Knappenberger, T., M. Flury, J. B. Harsh, E. Mattson, Using a Geocentrifuge to Study Colloid Transport in Unsaturated Porous Media, University of Hohenheim, Germany, May 3, 2012.

4. Knappenberger, T., M. Flury, J. B. Harsh, E. Mattson, Z. F. Zhang, G. W. Gee, P. Lichtner, Identifying the Role of Flow Rate and Water Content in Colloid Transport in Unsaturated Porous Media, EGU Annual Meeting in Vienna, Austria, April 22-27, 2012.

5. Knappenberger, T., M. Flury, J. B. Harsh, E. Mattson Z. F. Zhang, G. W. Gee, P. Lichtner, Using a Geocentrifuge to Study Colloid Transport in Unsaturated Porous Media, Soil Science Society Annual Meeting Annual Meeting, San Antonio, Oct 16-19, 2011.

6. Zhang. Z. F., C. E. Strickland, M. Flury, Z. Liu, G. W. Gee, J. B. Harsh, R. Clayton, Colloid-Facilitated Radionuclide Transport under Field Conditions at Hanford Washington, W1288 Regional Technical Committee Annual Meeting, Honolulu, Hawaii, Jan 2-5, 2012.

7. Cloy, J., M. Flury, J. B. Harsh, and J. B. Boyle, Interactions between Hanford Colloids and Humic Substances: Sorption Mechanisms and Colloid Stabilization, 15th International Humic Substances Society Meeting (IHSS15) on "Humic Substances and the Maintenance of Ecosystem Services", Puerto de la Cruz, Canary Islands, Spain, June 17-July 2, 2010.

8. Flury, M., J. B. Harsh, E. Mattson, Z. F. Zhang, G. W. Gee, P. Lichtner, Colloid Mobilization and Colloid-Facilitated Transport of Radionuclides in a Semi-Arid Vadose Zone, W1288 Regional Technical Committee Annual Meeting, Las Vegas, Jan 2-5, 2010.

9. Stickland, C., F. Zhang, G. Gee, M. Flury, and J. B. Harsh, Field Lysimeters to Study Colloid Transport at the Hanford Site. Annual Meeting of the Soil Science Society of America, Pittsburgh, November 2009.

10. Flury, M., Unresolved Issues in Colloid Transport in Unsaturated Porous Media. Annual Meeting of the Soil Science Society of America, Pittsburgh, November 2009.

11. Flury, M., On the Role of the Liquid-Gas Interface for Colloid Transport in Unsaturated Porous Media. Department of Chemical Engineering, Louisiana State University, Baton Rouge, April 2009.

12. Shang, J., M. Flury, and Y. Deng, Force measurements between particles and the air-water interface: Implications for particle mobilization in unsaturated porous media, *Water Resour. Res.*, *45*, W06420, doi:10.1029/2008WR007384, 2009.

13. Flury, M., Colloid Transport in Unsaturated Porous Media. Environmental Science and Research (ESR), Christchurch, New Zealand, January 2009.

### 4.4 Web Sites

The following web sites provide information about the project. The general web site is
`http://akasha.wsu.edu`.
A list of publication is given at
`http://akasha.wsu.edu/~flury/publications.html`.
Project information is given at
`http://akasha.wsu.edu/~flury/research/colloid2.html`.

## Appendix: Reprints of Publications

- Liu, Z., M. Flury, Z. F. Zhang, J. B. Harsh, G. W. Gee, C. E. Strickland, R. E. Clayton, Transport of Europium Colloids in Vadose Zone Lysimeters at the Semi-Arid Hanford Site, submitted to *Environ. Sci. Technol.*, 2012.

- Liu, Z., M. Flury, J. B. Harsh, J. B. Mathison, C. Vogs, Long-Term Water Flow and Colloid Transport in an Undisturbed Sediment Core at the Hanford Site, submitted to *Water Resources Research*, 2012.

- Chatterjee, N., S. Lapin, and M. Flury, Capillary forces between sediment particles and an air-water interface, *Environ. Sci. Technol.*, *46*, 4411–4418, 2012.

- Aramrak, S., M. Flury, and J. B. Harsh, Detachment of deposited colloids by advancing and receding air-water interfaces, *Langmuir*, *21*, 9985–9993, 2011.

- Shang, J., M. Flury, J. B. Harsh, and R. L. Zollars, Contact angles of aluminosilicate clays as affected by relative humidity and exchangeable cations, *Colloids Surf. Physicochem. Eng. Aspects*, *353*, 1–9, 2010.

- Mattson, E. D., C. D. Palmer, R. W. Smith, and M. Flury, Centrifuge techniques and apparatus for transport experiments in porous media, in *Physical Modelling in Geotechnics*, edited by Springman, Laue, and Seward, pp. 1465–1470, Taylor and Francis Group, London, 2010.

- Shang, J., M. Flury, and Y. Deng, Force measurements between particles and the air-water interface: Implications for particle mobilization in unsaturated porous media, *Water Resour. Res.*, *45*, W06420, doi:10.1029/2008WR007384, 2009.

- Shang, J., M. Flury, J. B. Harsh, and R. L. Zollars, Comparison of different methods to measure contact angles of soil colloids, *J. Colloid Interface Sci.*, *328*, 299–307, 2008.